Star-disk magnetospheric interaction and trends in the angular momentum transport

Miljenko Čemeljić

Nicolaus Copernicus Astronomical Center of the Polish Academy of Sciences, Warsaw, Poland

&

Academia Sinica Institute of Astronomy and Astrophysics, Taipei, Taiwan

Outline

- Introduction
- Analytical thin HD disk solution
- Numerical simulations in HD and MHD
- “Atlas” of solutions
- Trends in the angular momentum flux
- Expressions for physical quantities
- Outflows and “jets”
- Long-lasting simulations
- Other geometries of magnetic field
- Light curve hiccups
- Summary

Introduction

- First numerical solution of (HD) accretion disk was by Prendergast & Burbidge (1968)
- Analytical solution was given by Shakura & Sunyaev (1973)
- … (lots of good things, but mostly with 1D, vertically averaged models)
- In Kita (1995, PhD Thesis) and Kluźniak & Kita (2000, KK00) was given a solution of the thin HD polytropic disk in the full 3D. It was obtained by the method of asymptotic approximation with the disk thickness as a small parameter.
- In 2009, numerical simulations of star-disk magnetospheric interaction were done in 2D-axisymmetric simulations, by Romanova et al. (2009, 2013, with non-public code), Zanni & Ferreira (2009, 2013, with the publicly available PLUTO code).
- Development of disk simulations went in the direction of MRI in the disk (Flock et al. 2012) or radiative transfer simulations.
- In Čemeljić (2019), A&A, 624, A31, I repeated the Zanni et al. (2009, 2013) 2D axisymmetric viscous & resistive MHD simulations with PLUTO (ver. 4.1), and went on to a parameter study, to investigate the influence of different parameters.

Status when I started with ZEUS star-disk simulations

Table 1
In Many Resistive MHD Simulations Performed To Date, Assumptions for the Initial Conditions Vary Significantly and the Duration of Simulations is Very Different

	Ω_*	Corona	$\kappa = \rho_d/\rho_c$	$T_{\max}/T_0$ (days)	Resistive	Viscous
Hayashi et al. (1996)	Non-rotating	Non-rotating	10^3	5	Yes	No
Hirose et al. (1997)	Non-rotating	Rotating	10^4	16.5	Yes	No
		Rotating different than disk				
Miller & Stone (1997)	Slow	Solid body rotation	10^2	0.3	Yes	No
		Corotating with star at $R_{\rm cor}$				
Goodson et al. (1999)	Fast	Rotating	10^4	100	Yes	No
Romanova et al. (2002)	Slow	Corotating with star	10^2	100	No	Yes
		for $R \leqslant R_{\rm cor}$, else with disk				
Küker et al. (2003)	Slow	Not in hydrostatic balance,	10^3	1000	Yes	Yes
		non-rotating				
Ustyugova et al. (2006)	Fast	Corotating with star	10^3	2000	Yes	Yes
		for $R \leqslant R_{\rm cor}$, else with disk				
Romanova et al. (2009)	Fast	Corotating with star	10^4	2000	Yes	Yes
	and slow	for $R \leqslant R_{\rm cor}$, else with disk				
M. Čemeljić et al. (present paper)	Slow	Corotating with star	10^4	1500	Yes	No
		for $R \leqslant R_{\rm cor}$, else with disk				

Notes. We list some of the important works to put our work in context. In the second column, "fast" stellar rotation means that the corotation radius is smaller than the disk truncation radius, $R_{\rm cor} < R_t$, and "slow" rotation means that $R_{\rm cor} > R_t$. The disk is rotating in all the cases. The columns about physical resistivity and viscosity specify only if the option is included in the code at all; for where it is really effective, reader should check the related publication. When present, viscosity is important only in the disk.

ZEUS simulations results-microejections

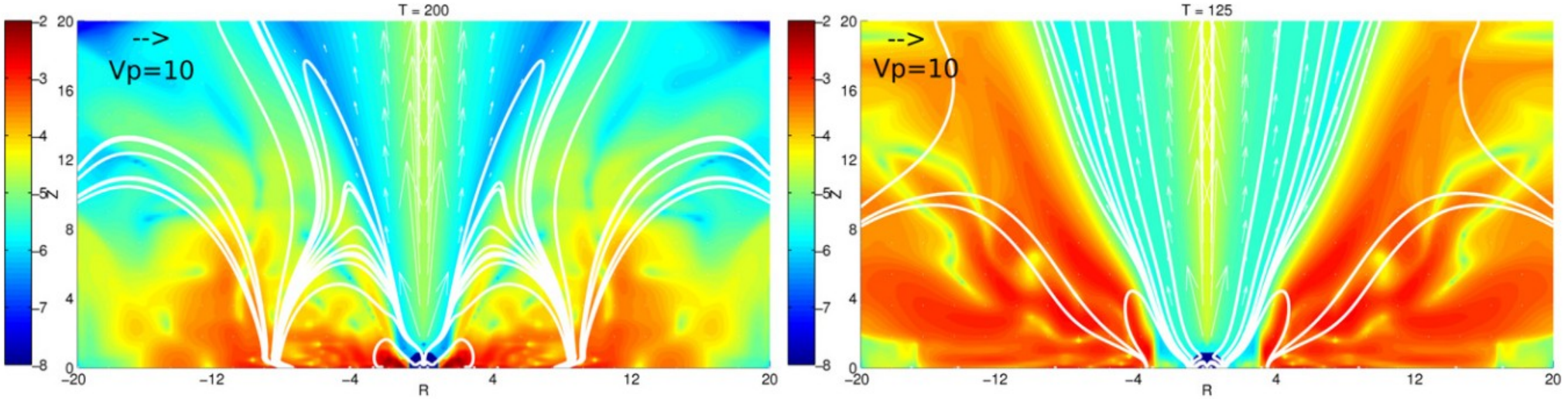

Figure 5. Mass flux ρv for the case with medium magnetic field in simulation S1a is shown in the left panel, and in simulation S1b, with larger magnetic field, in

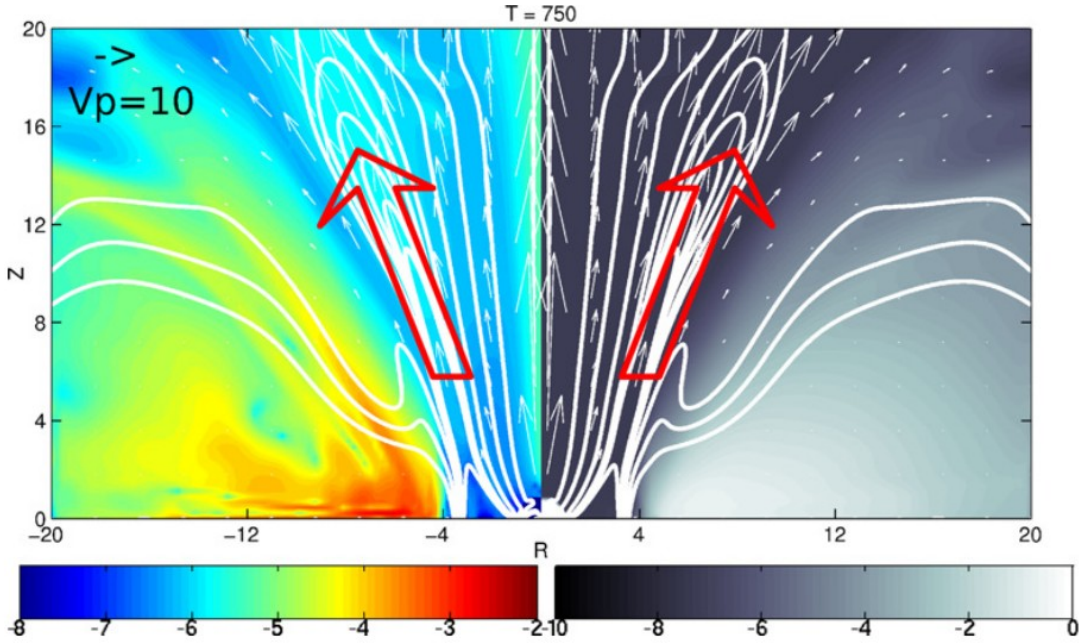

simulation S2. The left half of each panel shows the poloidal mass flux ρv_p, and the right half shows the density.

ZEUS results-effects of anomalous resistivity

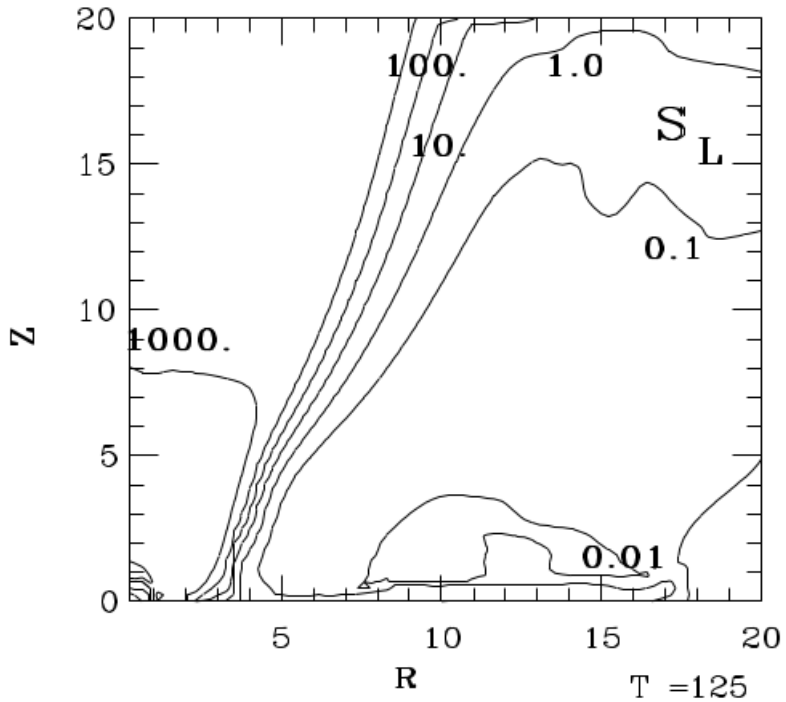

Figure 23. Isocontours of the Lundquist number S_L in S1b, at $T = 125$. Values of S_L for some isocontours are labeled on the plot.

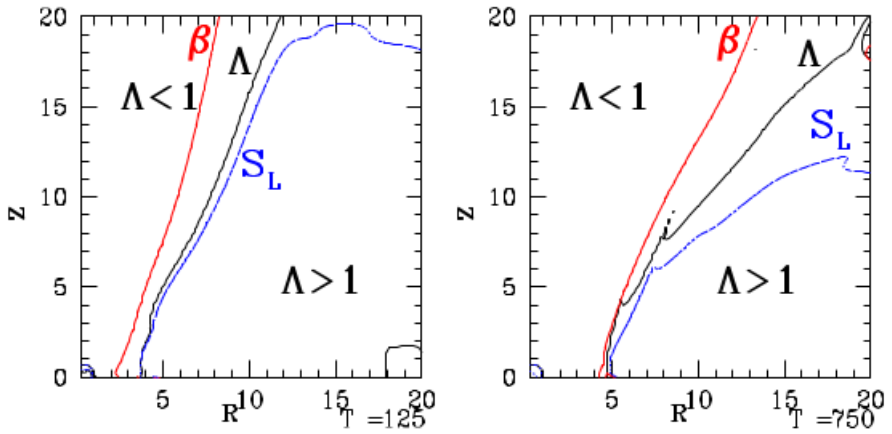

Figure 24. Elsässer number Λ is shown by the thick (black) solid line at $T = 125$ and $T = 750$ in simulations S1b and S2, in the left and right panels, respectively. Above the line in the computational box where magnetic pressure equals matter pressure ($\beta = 1$), and where the Elsässer number Λ equals unity (red solid line), launching of a flow of matter is possible. Below those lines, the

The electrical resistivity η is defined through the electric conductivity σ as $\eta = c^2/4\pi\sigma$, where c is the speed of light. The ratio of the advection and diffusion terms in the induction Equation (3) is the magnetic Reynolds number $\mathrm{Rm} = VL/\eta$, where V and L stand for the characteristic speed and distance, respectively. The characteristic speed in our problem is the Alfvén speed $v_A = B/(4\pi\rho)^{1/2}$, which defines the Lundquist number[4] S_L:

$$S_L = \frac{v_A L}{\eta}. \tag{18}$$

To explain the physical processes, the accretion disk requires an enhanced, *anomalous* level of resistivity, which is much larger

Another number that we find to indicate where the launching is possible from is the Elsässer number. It is defined by the ratio of the Z-component of the Alfvén velocity and $\eta\Omega_K$ (see Salmeron et al. 2007 and references therein):

$$\Lambda \equiv \frac{V_{AZ}^2}{\eta\Omega_K} > 1. \tag{21}$$

In some systems, when the flow is mainly in the Z-direction, Λ can be similar or equal to the Lundquist number S_L or the magnetic Reynolds number Rm, but, in general, they are different because the velocity of the outflow differs from the Alfvén velocity.

In Figure 24, we plot the Elsässer number $\Lambda > 1$ in simulations S1b and S2. We observe that $\Lambda \geqslant 1$ is valid only in the magnetosphere above the disk. For a small magnetic field of

Kluźniak-Kita thin disk analytical solutions

Initial conditions are HD disk and a hydrostatic corona. Examples from derivation:

Equation of continuity:

$$\frac{\epsilon}{r}\frac{\partial}{\partial r}\left(r\rho v_r\right)+\frac{\partial}{\partial z}\left(\rho v_z\right)=0 \tag{1}$$

Order ϵ^0:

$$\frac{\partial}{\partial z}\left(\rho_0 v_{z0}\right)=0 \;\Rightarrow v_{z0}=0 \tag{2}$$

Order ϵ^1:

$$\frac{1}{r}\frac{\partial}{\partial r}\left(r\rho_0 v_{r0}\right)+\frac{\partial}{\partial z}\left(\rho_0 v_{z1}\right)=0 \tag{3}$$

From the argumentation presented below, for the first order in ϵ of the radial momentum, we have $v_{r0}=0$, so that here we have $\partial_z(\rho_0 v_{z1})=0 \Rightarrow \rho_0 v_{z1}=const$ along z. Since v_z is odd with respect to z, at the disk equatorial plane it is $\rho_0 v_{z1}=0$. Since it does not depend on z, and $\rho_0\neq 0$, we conclude that $v_{z1}=0$.

Order ϵ^2:

$$\frac{1}{r}\frac{\partial}{\partial r}\left(r\rho_0 v_{r1}\right)+\frac{\partial}{\partial z}\left(\rho_0 v_{z2}\right)=0 \tag{4}$$

Vertical momentum:

$$\begin{aligned}\epsilon v_r\frac{\partial v_z}{\partial r}+v_z\frac{\partial v_z}{\partial z}=&-\frac{z}{r^3}\left[1+\epsilon^2\left(\frac{z}{r}\right)^2\right]^{-3/2}\\ -n\frac{\partial c_s^2}{\partial z}&+\frac{2}{\gamma\tilde{\beta}}\frac{1}{\rho}\left(\epsilon B_r\frac{\partial B_z}{\partial r}+B_z\frac{\partial B_z}{\partial z}\right)-\frac{1}{\gamma\tilde{\beta}}\frac{1}{\rho}\frac{\partial B^2}{\partial z}\\ &+\frac{2}{\rho}\frac{\partial}{\partial z}\left(\eta\frac{\partial v_z}{\partial z}\right)+\frac{\epsilon^2}{\rho r}\frac{\partial}{\partial r}\left(r\eta\frac{\partial v_z}{\partial r}\right)\\ &-\frac{2}{3}\frac{\epsilon}{\rho}\frac{\partial}{\partial z}\left(\frac{\eta}{r}\frac{\partial}{\partial r}\left(rv_r\right)\right)-\frac{2}{3\rho}\frac{\partial}{\partial z}\left(\eta\frac{\partial v_z}{\partial z}\right)\\ &+\frac{\epsilon}{\rho r}\frac{\partial}{\partial r}\left(\eta r\frac{\partial v_r}{\partial z}\right)\end{aligned} \tag{17}$$

Order ϵ^0:

$$0=-\frac{z}{r^3}-n\frac{\partial c_{s_0}^2}{\partial z}-\frac{1}{\gamma\tilde{\beta}}\frac{1}{\rho_0}\frac{\partial B_0^2}{\partial z} \tag{18}$$

Since we had $\partial B_{r0}/\partial z=\partial B_{z0}/\partial z=\partial B_{\varphi 0}/\partial z=0$, we have $\partial B_0/\partial z=0$, i.e. $B_0=f(r)$. We have then

$$\frac{z}{r^3}=-n\frac{\partial c_{s_0}^2}{\partial z}, \tag{19}$$

which is the vertical hydrostatic equilibrium equation, with the solution in the case of $n=3/2$:

$$c_{s0}=\sqrt{\frac{h^2-z^2}{3r^3}},\;\rho_0=\left(\frac{h^2-z^2}{5r^3}\right)^{3/2}, \tag{20}$$

where h is the semi-thickness of the disk. This also gives us the pressure relation $P=\rho_0^{5/3}=[(h^2-z^2)/5r^3]^{5/2}$ (Hoshi 1977; Kluźniak & Kita 2000).

Numerical setup

•I perform simulations of a rotating thin accretion disk, which reach a quasi-stationary state.

•Ohmic and viscous heating in the energy equation are neglected, assuming that all the heat is radiated away.

•Viscosity and resistivity are still included, in the equation of motion and in the induction equation.

•Code used is PLUTO (v.4.1) by Mignone et al. (2007).

$$\frac{\partial \rho}{\partial t} + \nabla \cdot (\rho \boldsymbol{u}) = 0$$

$$\frac{\partial \rho \boldsymbol{u}}{\partial t} + \nabla \cdot \left[\rho \boldsymbol{u}\boldsymbol{u} + \left(P + \frac{\boldsymbol{B} \cdot \boldsymbol{B}}{8\pi} \right) \boldsymbol{I} - \frac{\boldsymbol{B}\boldsymbol{B}}{4\pi} - \boldsymbol{\tau} \right] = \rho \boldsymbol{g}$$

$$\frac{\partial E}{\partial t} + \nabla \cdot \left[\left(E + P + \frac{\boldsymbol{B} \cdot \boldsymbol{B}}{8\pi} \right) \boldsymbol{u} - \frac{(\boldsymbol{u} \cdot \boldsymbol{B})\, \boldsymbol{B}}{4\pi} \right] + \nabla \cdot [\eta_{\mathrm{m}} \boldsymbol{J} \times \boldsymbol{B}/4\pi - \boldsymbol{u} \cdot \boldsymbol{\tau}] = \rho \boldsymbol{g} \cdot \boldsymbol{u} - \Lambda_{\mathrm{cool}}$$

$$\frac{\partial \boldsymbol{B}}{\partial t} + \nabla \times (\boldsymbol{B} \times \boldsymbol{u} + \eta_{\mathrm{m}} \boldsymbol{J}) = 0.$$

Hydro-dynamic star-disk analytical solutions and simulations

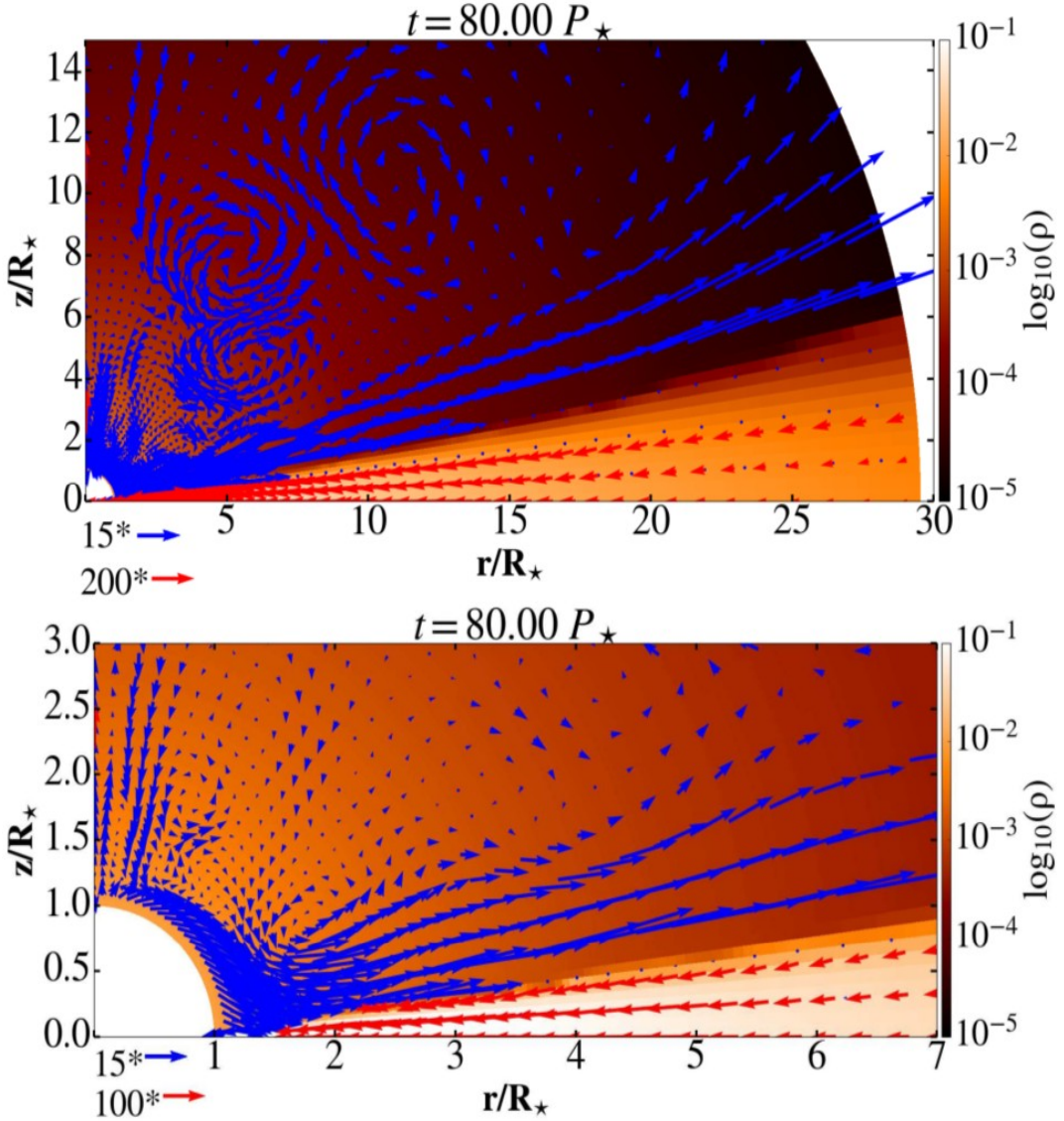

Computational box and a zoom closer to the star after 80 stellar rotations. In color is shown the density, and vectors show velocity, with the different normalization in the disk and stellar wind.

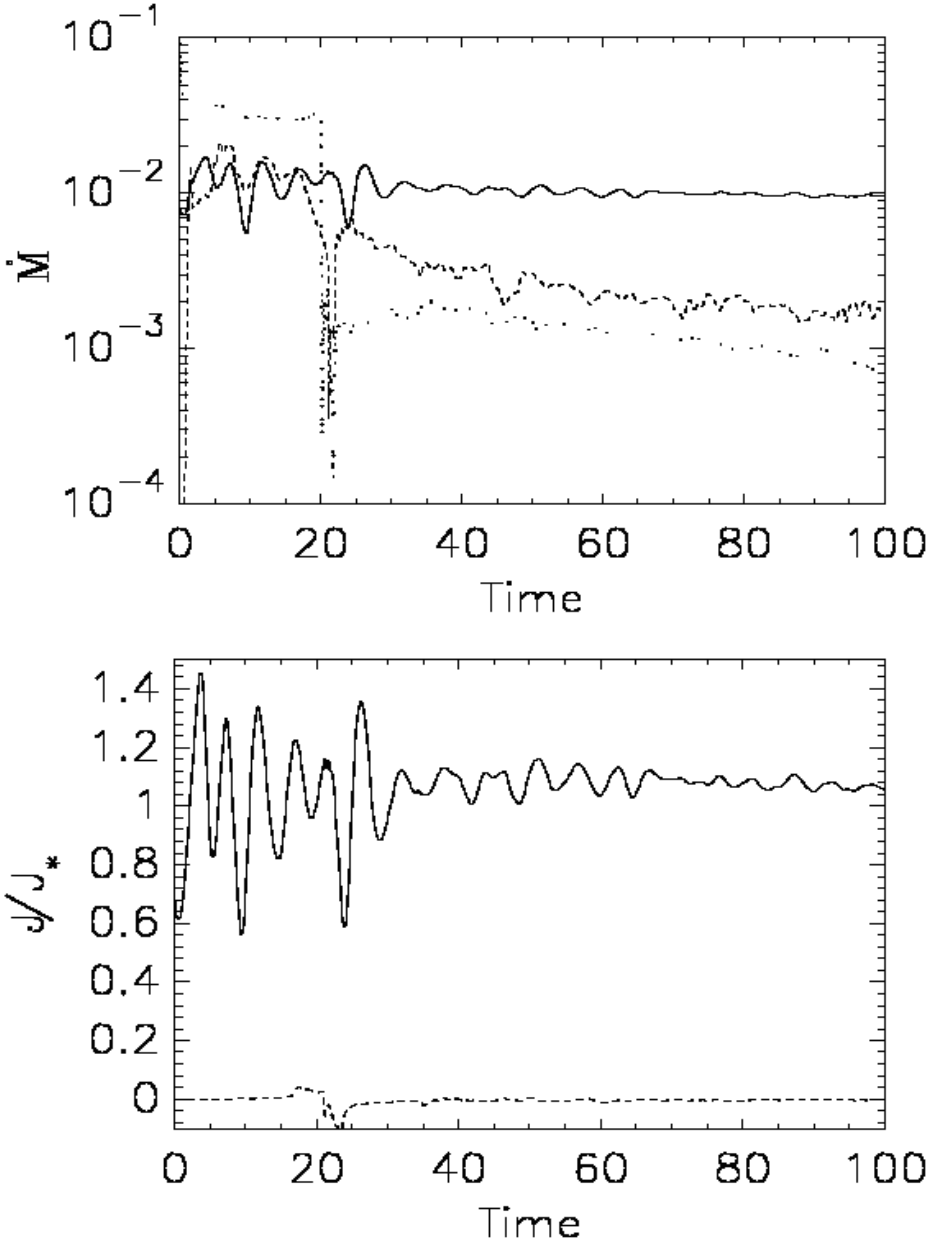

Time dependence of the mass and angular momentum fluxes in the various components in our simulations.

Star-disk simulations with magnetic field

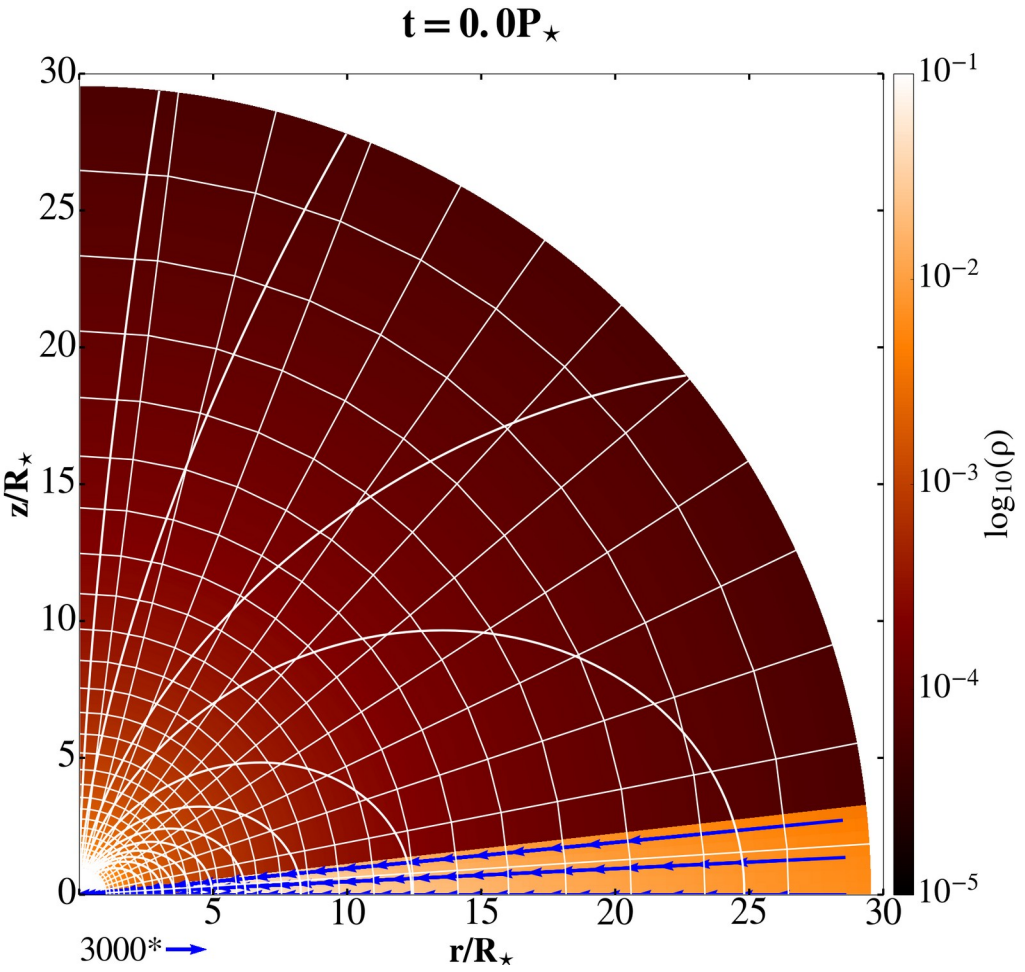

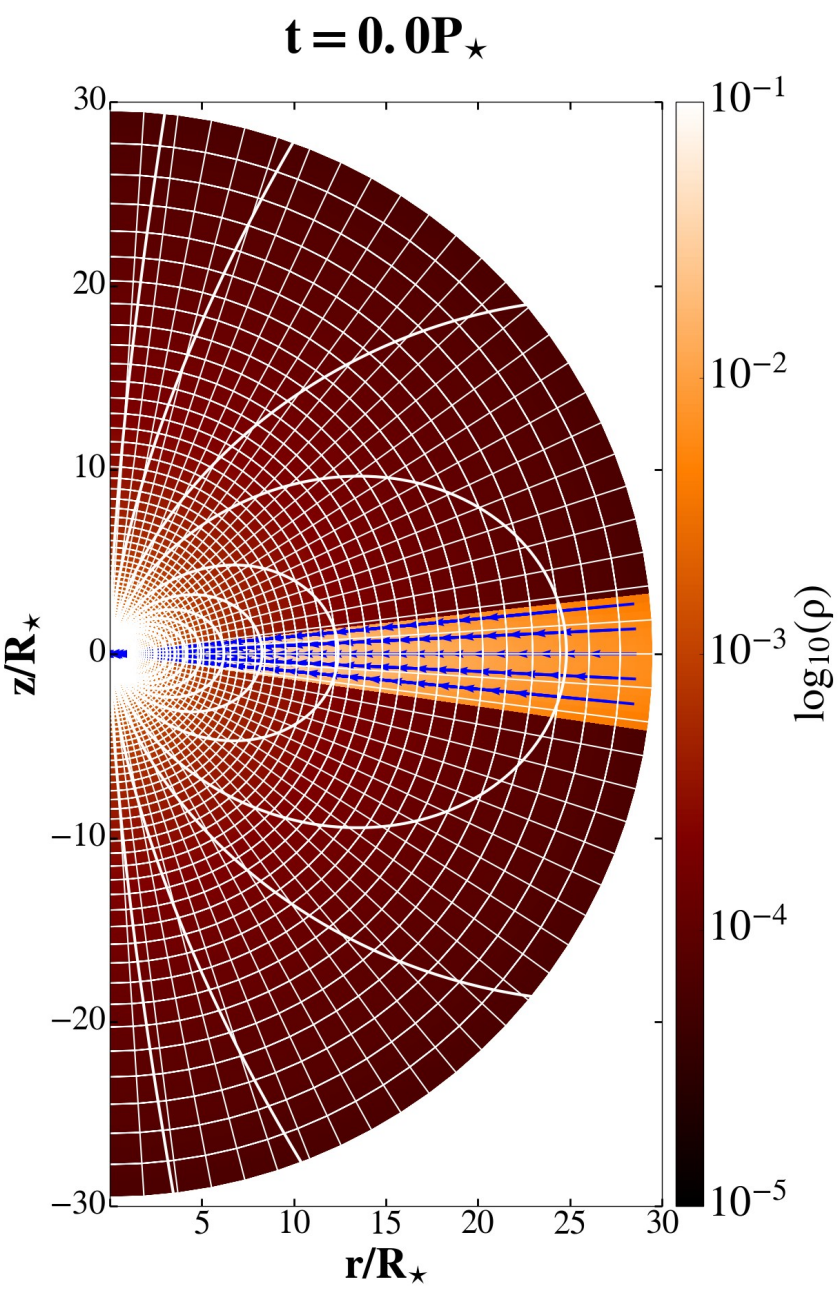

- We add the magnetic field to the HD solution
- Stellar surface is a rotating boundary condition at the origin of the spherical computational domain. We assume the star to be a magnetized rotator. The initially non-rotating corona is in a hydrostatic balance.

Star-disk simulations $\alpha_v=1.$

Table 1. The parameters in our study presented in the "Atlas": the stellar angular velocity $\Omega_\star$, stellar dipole magnetic field strength $B_\star$, and the magnetic Prandtl number $P_{\rm m}$-for which we also table the values of corresponding resistivity coefficient $\alpha_{\rm m}$. We show also the stellar rotation period, and corotation radius in young stellar object (YSO) cases.

$\Omega_\star/\Omega_{\rm br}$	$B_\star$(G)	$P_{\rm m}$	$\alpha_{\rm m}$	$P_\star$(days)	$R_{\rm cor}(R_\star)$
0.05	250	6.7	0.1	9.2	7.37
0.1	500	1.67	0.4	4.6	4.64
0.15	750	0.95	0.7	3.1	3.54
0.2	1000	0.67	1.0	2.3	2.92

- Prandtl magnetic number:

$$P_{\rm m} = \frac{2}{3}\frac{\alpha_{\rm v}}{\alpha_{\rm m}}$$

Star-disk simulations parameter space

Table 1. We performed 64 star-disk magnetospheric interaction simulations in a setup detailed in Čemeljić (2019). There are all together 64 runs with all the combinations of parameters as listed in the table. The magnetic Prandtl number $P_m = \frac{2}{3}\alpha_v/\alpha_m$ is also listed – in all the cases the anomalous viscosity parameter is $\alpha_v = 1$. The four simulations shown in Fig. 1 are highlighted with boxed bold letters.

$\alpha_m =$	0.1	0.4	0.7	1
$P_m =$	6.7	1.67	0.95	0.67
$\Omega_\star/\Omega_{br}$				
	$B_\star$=250 G			
0.05	a1	a2	a3	a4
0.1	a5	a6	a7	a8
0.15	a9	a10	a11	a12
0.2	a13	a14	a15	a16
	$B_\star$=500 G			
0.05	b1	b2	b3	b4
0.1	**b5**	b6	b7	**b8**
0.15	b9	b10	b11	b12
0.2	b13	b14	b15	b16
	$B_\star$=750 G			
0.05	c1	c2	c3	c4
0.1	c5	c6	c7	c8
0.15	**c9**	c10	c11	c12
0.2	c13	c14	c15	c16
	$B_\star$=1000 G			
0.05	d1	d2	d3	d4
0.1	d5	d6	d7	d8
0.15	d9	d10	d11	**d12**
0.2	d13	d14	d15	d16

I did a systematic study with magnetic star-disk numerical simulations in 64 points in parameter space, for a slowly rotating star, with

With PhD students in CAMK and in Taiwan, and with summer students, we continued this work, to go to the other parts of the parameter space and other geometries of magnetic field.

Sure, it would be better done in full 3D, but 2D axisymmetric results will not harm for a comparison, and will be faster available.

Star-disk magnetospheric interaction (SDMI) simulations

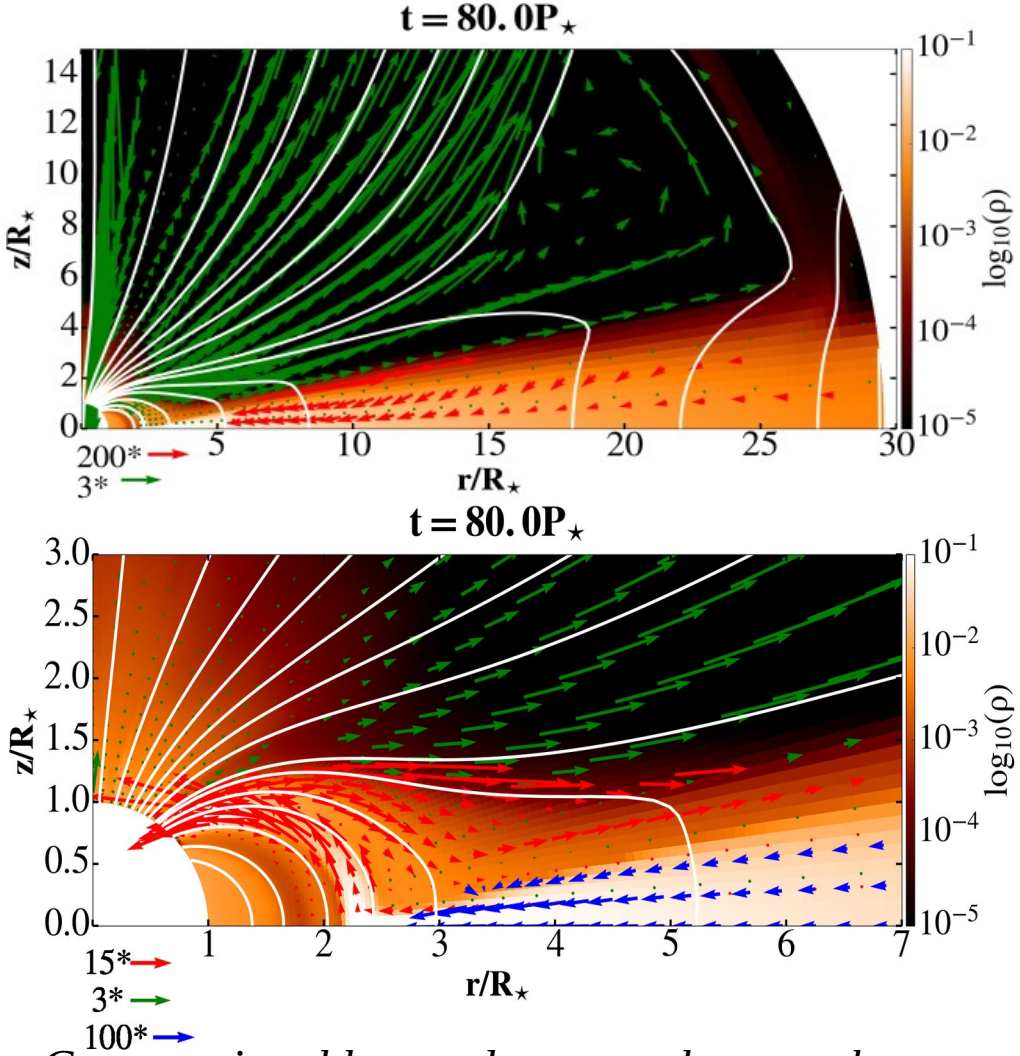

Computational box and a zoom closer to the star after 80 stellar rotations, to visualize the accretion column and the magnetic field lines (white solid lines), connected to the disk beyond the corotation radius Rcor=2.92 Rs. In color is shown the density, and vectors show velocity, with the different normalization in the disk, column and stellar wind.

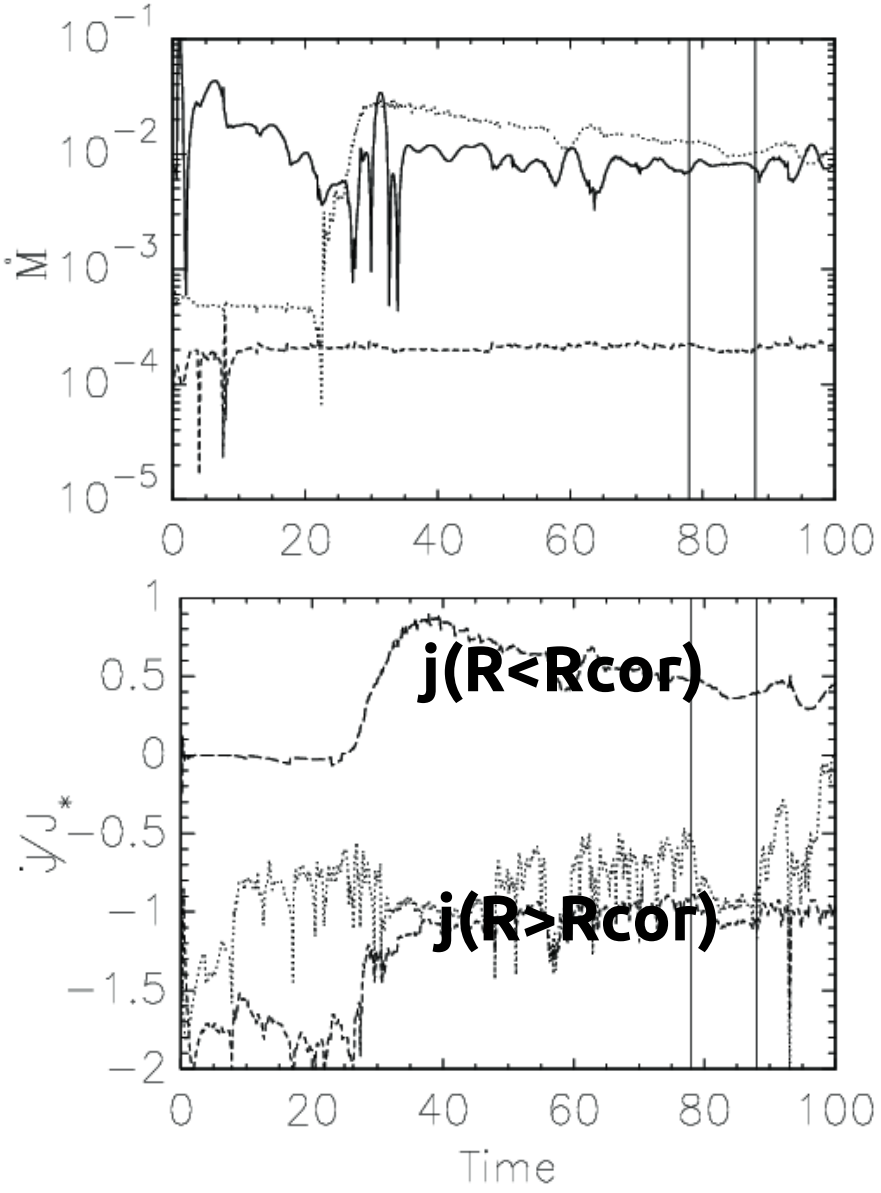

Time dependence of the mass and angular momentum fluxes in the various components in our simulations with marked the time interval in which the average for the quasi-stationarity is computed.

Part of the “Atlas” of solutions for 250 Gauss

Atlas2: Results for density (top panels) and poloidal momentum (bottom panels) in PLUTO simulations of star-disk magnetospheric interactions in different points in the parameter space. Collaborations with Ruchi Mishra (NCAC) and Aleksandra Kotek (Uni Warsaw, NCAC). MČ, April 2020.

$alpha_v$	0.2	0.2	0.2	0.2	0.4	0.4	0.4	0.4	1	1	1	1
$alpha_m$	0.1	0.4	0.7	1	0.1	0.4	0.7	1	0.1	0.4	0.7	1
Pm	1.33	0.33	0.19	0.13	2.67	0.67	0.38	0.63	6.67	1.67	0.95	0.67
B_*=250 Gauss												
$Omega_*$												
0.05									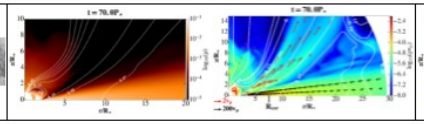	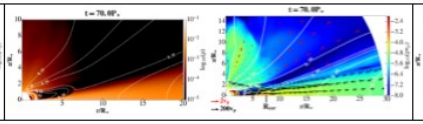	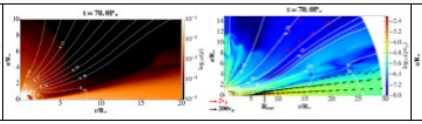	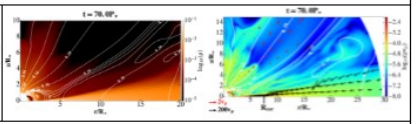
0.1									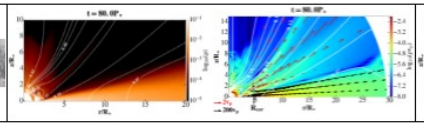	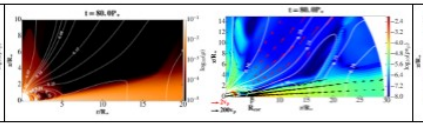	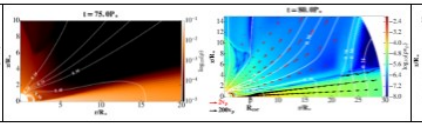	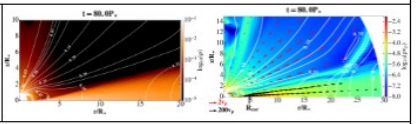
0.15									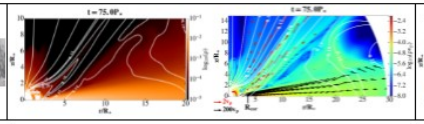	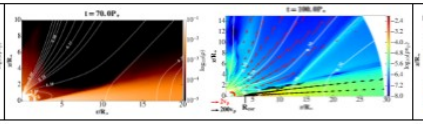	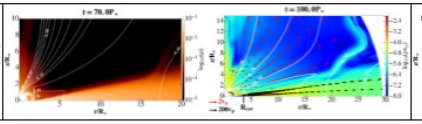	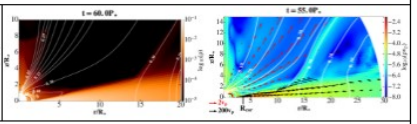
0.2									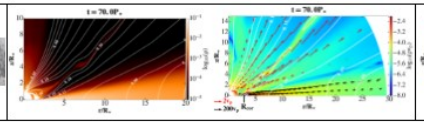	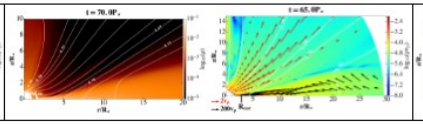	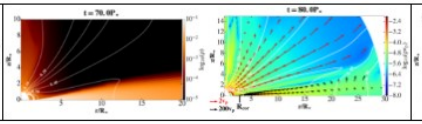	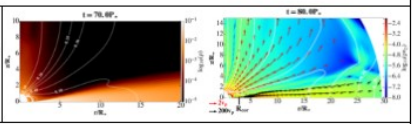
0.4												
0.6												

Example of a solution with 500 Gauss

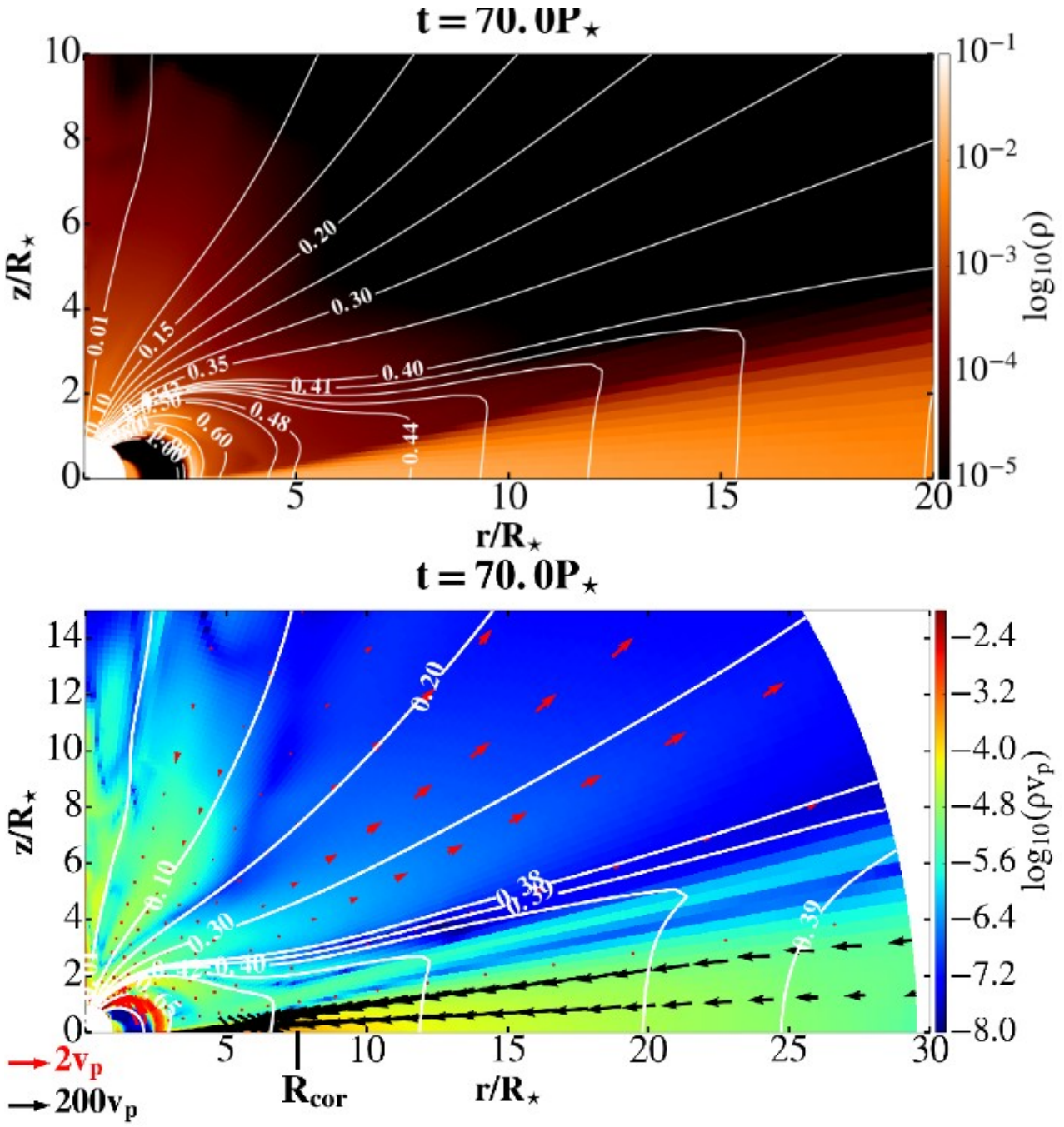

Configurations of solutions in “Atlas”

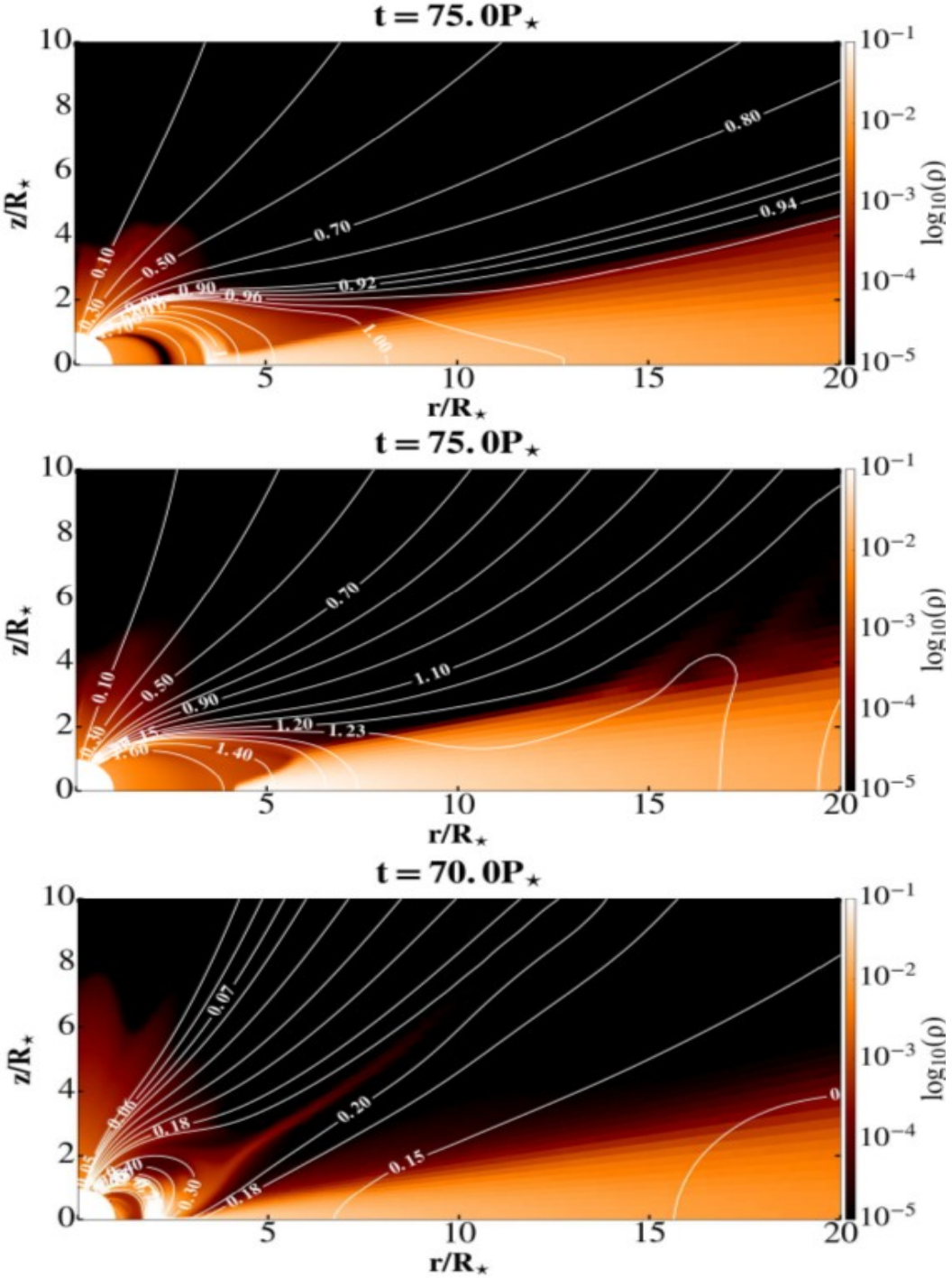

Table 2. Parameter space in the simulations, with an “Atlas” of solutions, where the geometry of the flow components in each case is labeled with D for disk, DC for disk+column, and DCE for disk+column+ejection.

α_m =	0.1	0.4	0.7	1
$\Omega_\star/\Omega_{br}$				
	$B_\star$ = 250 G			
0.05	DCE	DC	DC	DC
0.1	DCE	DC	DC	DC
0.15	DCE	DC	DC	DC
0.2	DCE	DC	DC	DC
	$B_\star$ = 500 G			
0.05	DCE	DC	DC	DC
0.1	DCE	DC	DC	DC
0.15	DCE	DC	DC	DC
0.2	DCE	DC	DC	DC
	$B_\star$ = 750 G			
0.05	DCE	DC	DC	DC
0.1	DCE	DC	DC	DC
0.15	DCE	DC	DC	DC
0.2	DCE	DC	DC	DC
	$B_\star$ = 1000 G			
0.05	DCE	DC	DC	DC
0.1	DCE	DC	DC	DC
0.15	DCE	D	D	D
0.2	DCE	D	D	D

- Three different cases of geometry in our results: top and middle panels B=1 kG and α_m=1, in the cases with Ω_s=0.1 and Ω_s=0.15, bottom panel B=0.5kG, α_m=0.1,Ω_s=0.1.

Configurations of solutions in “Atlas”

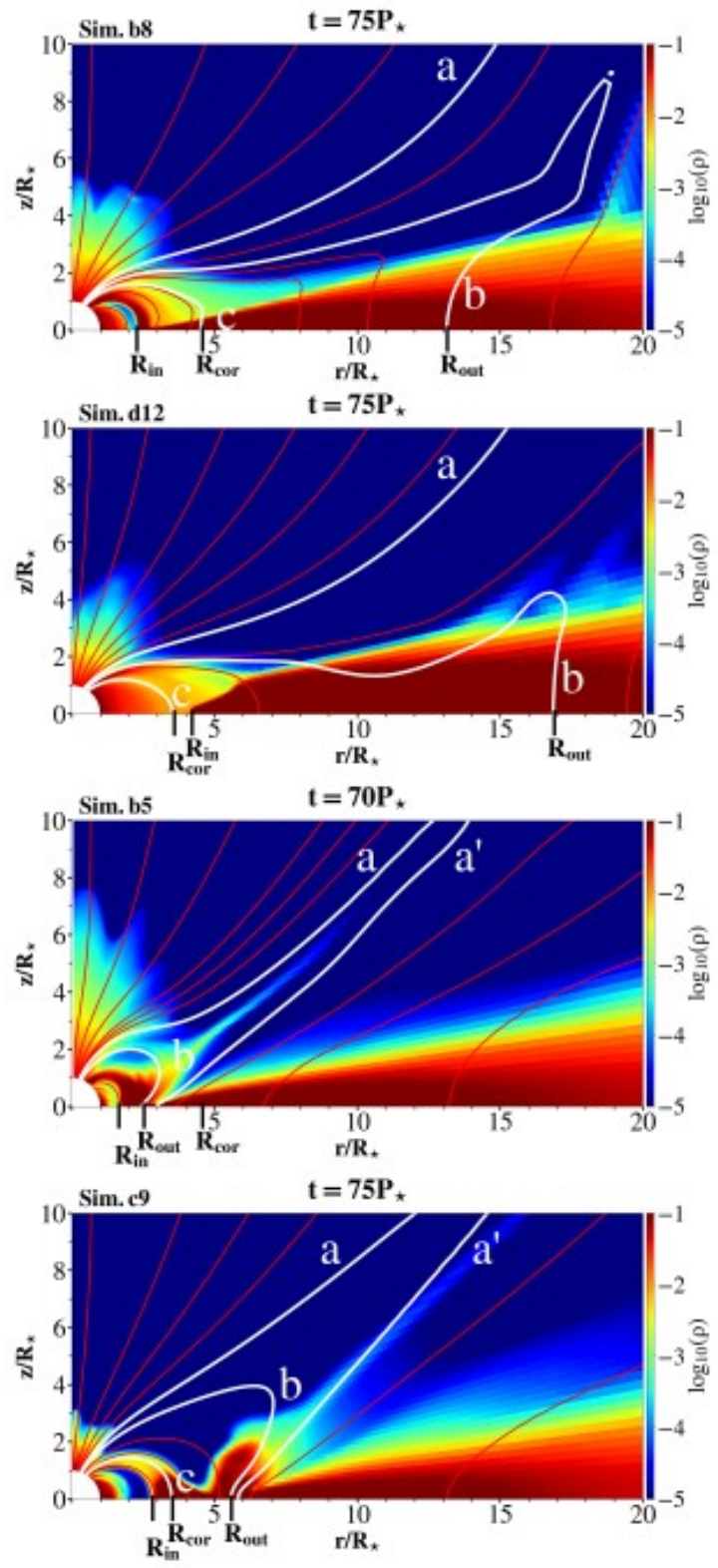

- 4 different cases if we consider the position of Rcor in the case with conical outflow.
- In general, faster stellar rotation prevents the accretion column formation.
- In the bottom panels resistivity α_m=0.1 and Ω_s=0.1, a conical outflow is formed.

Comparison of SDMI simulations with increasing mag. field

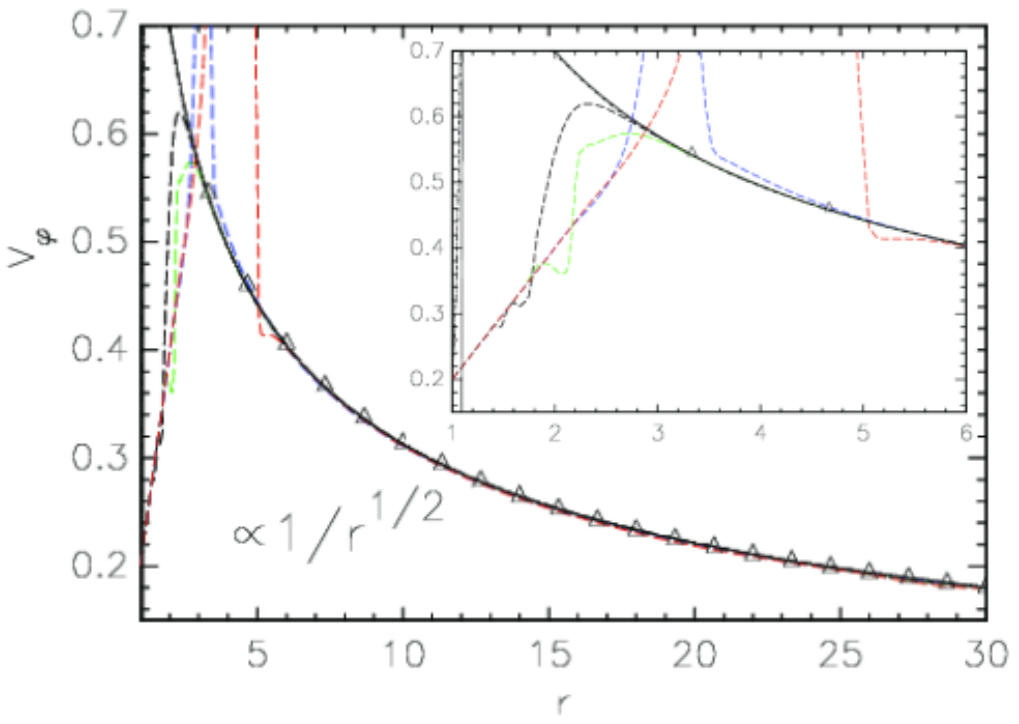

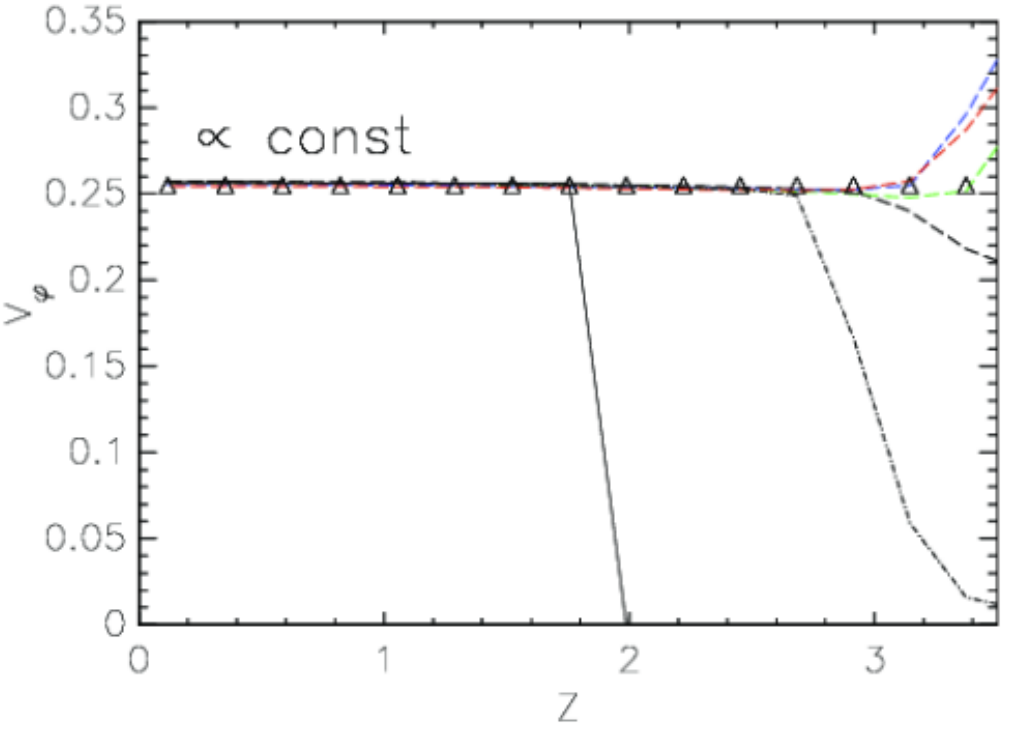

Fig. 2. The azimuthal velocity of thin discs from our simulations with $\Omega = 0.2\,\Omega_{\rm ms}$. As expected from theory, it closely follows the Keplerian curve and is uniform on cylinders (with corrections of order z^2/r^2). The disc-corona interface is at $z \approx 2$. In this and later figures, shown are values in the initial set-up (thin solid line) with the quasi-stationary solutions in the numerical simulations in the HD (dot-dashed line) and the MHD (long-dashed line) cases. In black, green, blue and red colors are the results in the MHD cases with the stellar magnetic field strength $(0.35,\ 0.7,\ 1.05,\ 1.4)B_0$, respectively. The closest match to the $0.7B_0$ case is depicted with triangle symbols. *Left panel:* radial dependence along the midplane, just above θ=90°. Insert shows a zoom into the vicinity of the stellar surface. *Right panel:* the profiles along a vertical line at r=$15R_\star$. The thin solid line in the right panel, sloping down at $z \approx 2$, indicates v_φ in the initial set-up.

Comparison of SDMI simulations with increasing mag. field

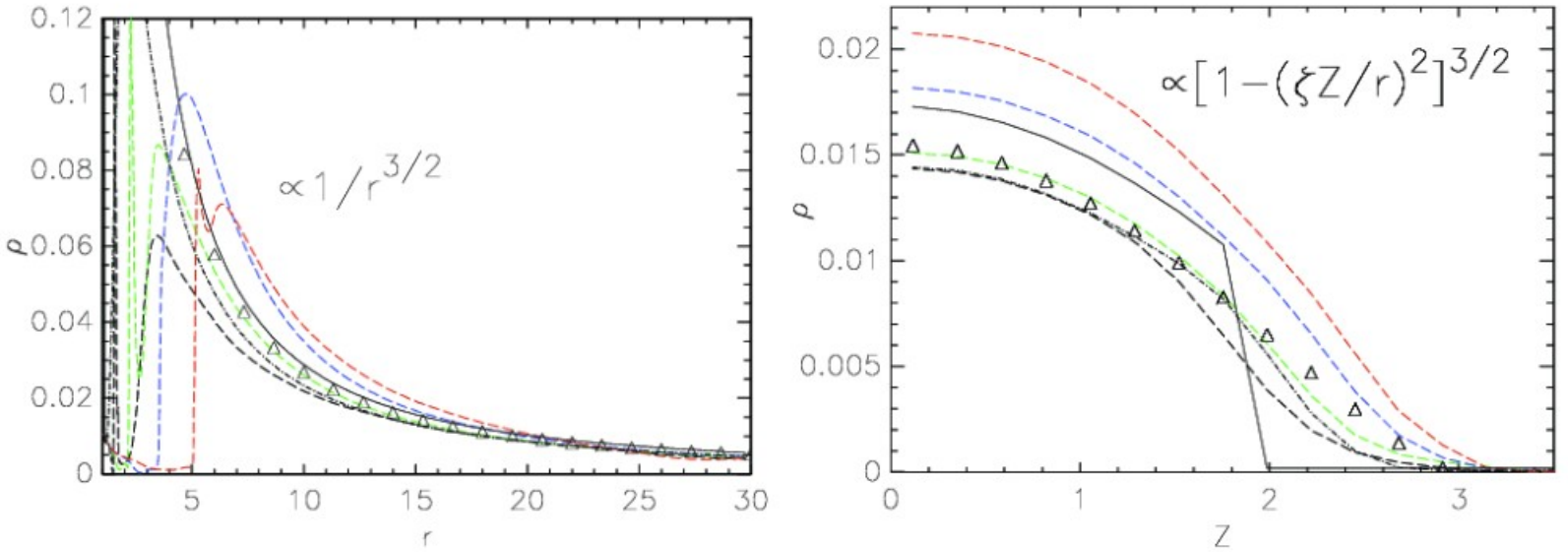

Fig. 3. Comparison of the matter density *Left panel:* radial dependence along the midplane, just above θ=90°. *Right panel:* the profiles along the vertical line at r=15$R_\star$. The legend is the same as in Fig. 2.

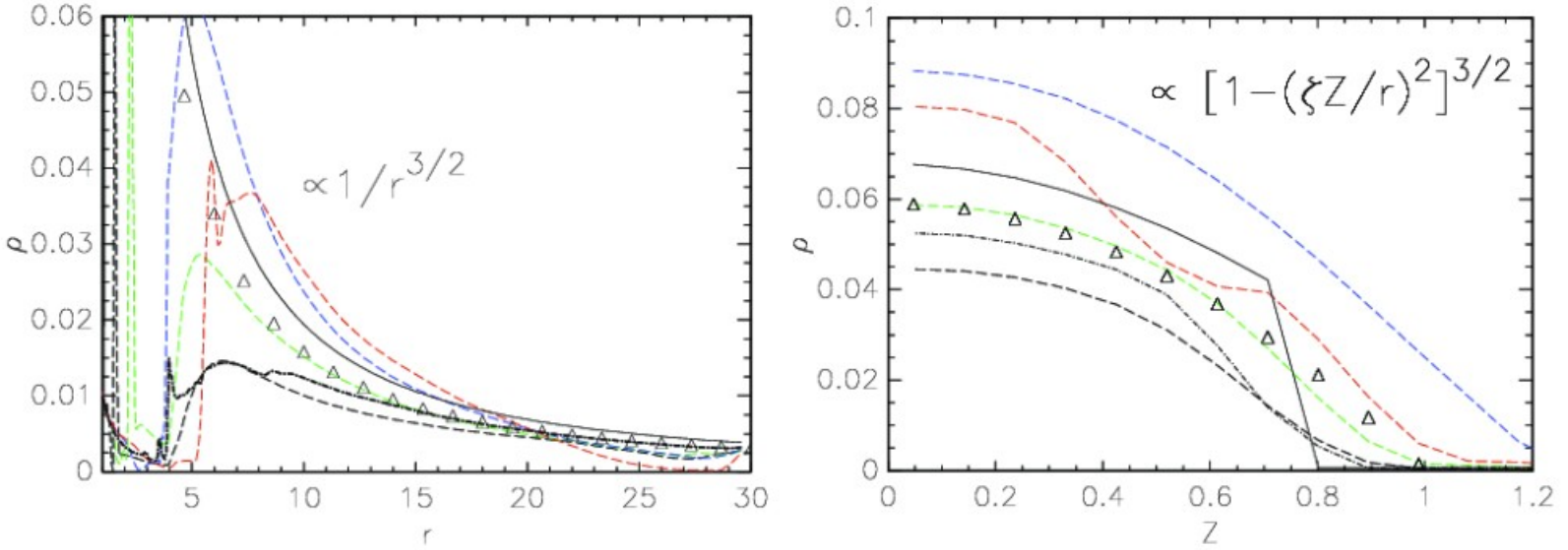

Fig. 4. Comparison of the matter density in the initial set-up (solid line) with the quasi-stationary solutions in numerical simulations in the HD (dot-dashed line) and the MHD cases. *Left panel:* along the disc surface at θ=83°. *Right panel:* along a vertical line at r=6$R_\star$. The meaning of the lines is the same as in Fig. 3.

Comparison of SDMI simulations with increasing mag. field

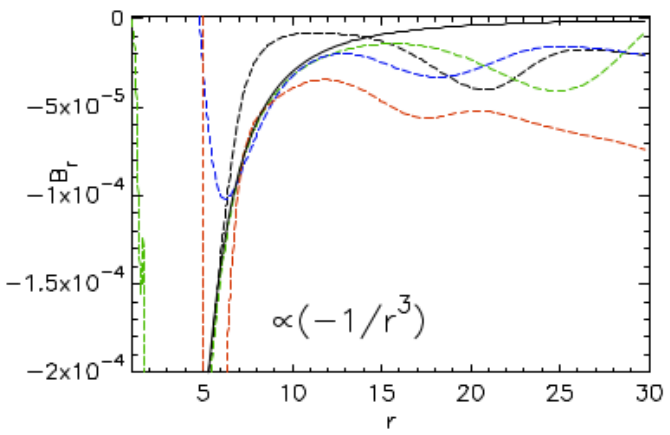

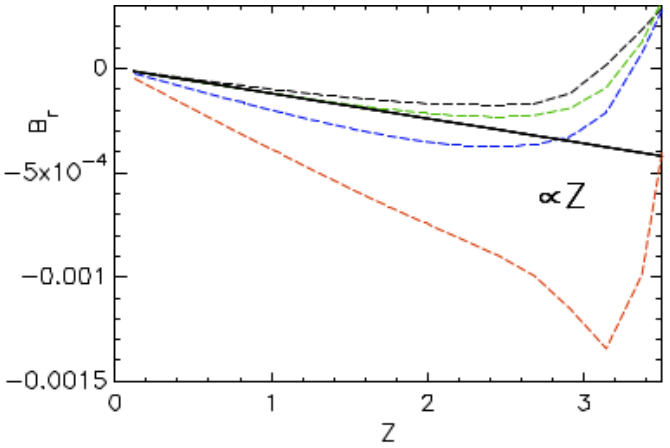

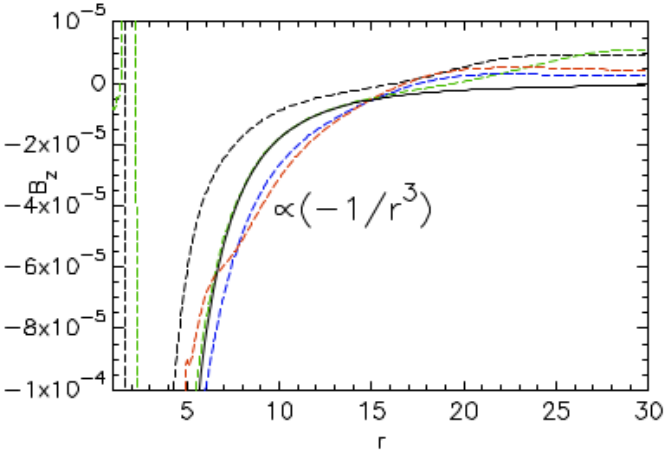

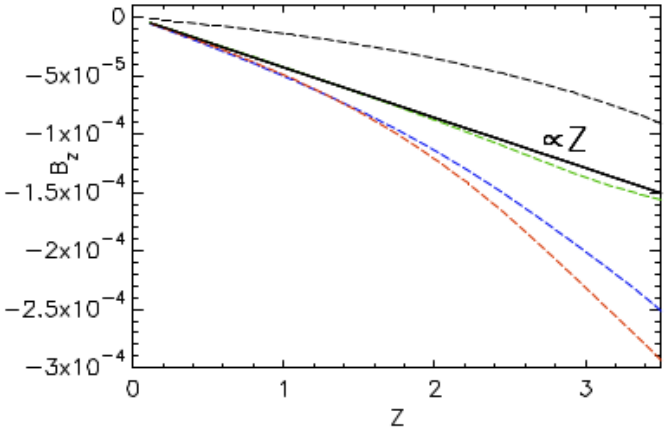

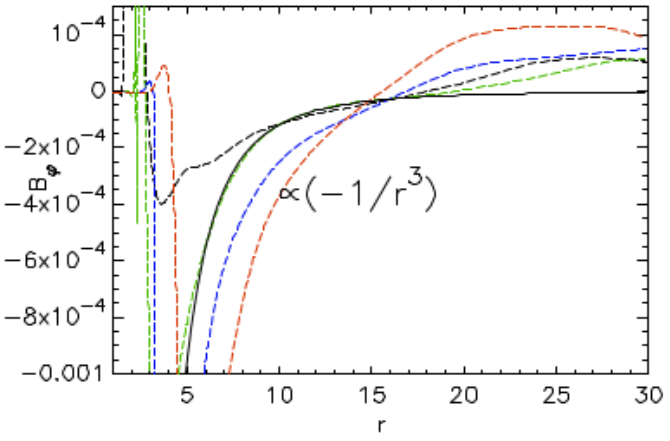

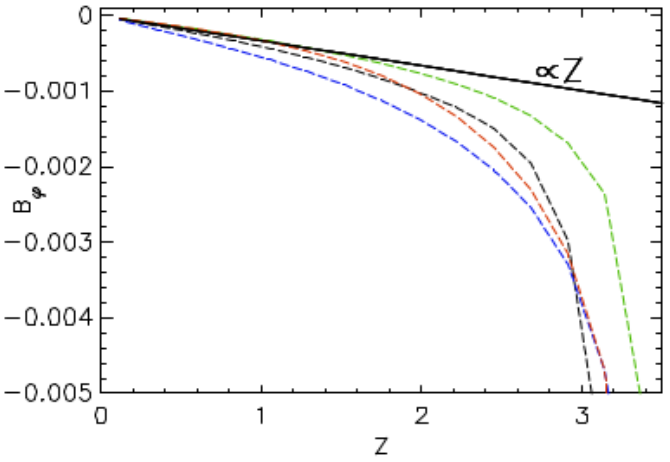

Comparison for magnetic field. In black, green blue and red colors are the results in the MHD cases with the stellar magnetic field strength 0.25, 0.5, 0.75 and 1.0 kG, respectively.

The closest fit to the 0.5 kG case is depicted with the thick solid line.

Trends in solutions with increasing stellar magnetic field

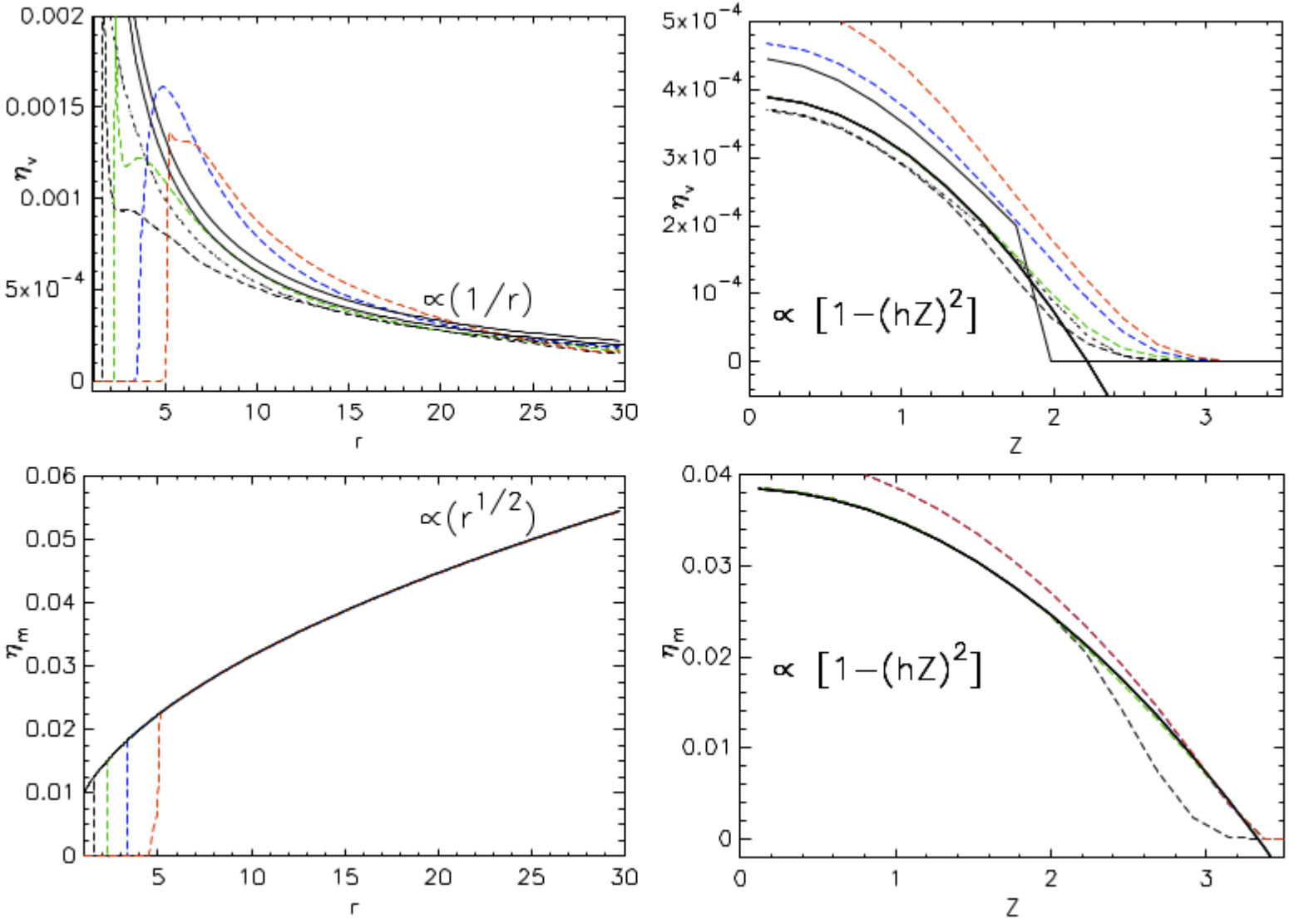

Comparison for diffusive coefficients. In black, green blue and red colors are the results in the MHD cases with the stellar magnetic field strength 0.25, 0.5, 0.75 and 1.0 kG, respectively. The closest fit to the 0.5 kG case is depicted with the thick solid line.

Expressions for physical quantities in the disk

We can write the results in our simulations as simple functions obtained in KK00, with coefficients of proportionality we find from our simulations:

$$\rho(r,z) = \frac{k_1}{r^{3/2}}\left[1-\left(\zeta_1\frac{z}{r}\right)^2\right]^{3/2}, \tag{69}$$

$$v_r(r,z) = \frac{k_2}{r^{1/2}}\left[1+(\zeta_2 z)^2\right], \tag{70}$$

$$v_z(r,z) \approx \frac{z}{r}v_r(r,z) = k_3\frac{z}{r^{3/2}}\left[1+(\zeta_3 z)^2\right],$$

$$v_\varphi(r,z) = \frac{k_4}{\sqrt{r}},\ \Omega = \frac{v_\varphi}{r} = \frac{k_4}{r^{3/2}}.$$

Magnetic field components are proportional to r^{-3}, as expected for the dipole stellar field, and depend linearly on height above the disk midplane:

$$B_r(r,z) = \frac{k_5}{r^3}z,\ B_z(r,z) = \frac{k_6}{r^3}z,\ B_\varphi(r,z) = \frac{k_7}{r^3}z, \tag{71}$$

$$\eta(r,z) = \frac{k_8}{r}\left[1-\left(\zeta_8\frac{z}{r}\right)^2\right]^2, \tag{72}$$

$$\eta_{\rm m}(r,z) = k_9\sqrt{r}\left[1-\left(\zeta_9\frac{z}{r}\right)^2\right]^{1/2}.$$

We assign the proportionality coefficients as $k_1, k_2, \ldots$ in the cases with a stellar dipole field of 500 G and 1000 G in Table 1, indicating by the additional subscripts i and o if they are given in the *inner* (R=6) or *outer* (R=15) position in the disk[4]. We also assign the corresponding coefficients $\zeta_1, \zeta_2, \ldots$ where needed.

In the following, we compare the above matches to solutions obtained in the simulations, with the conditions obtained from the analytical equations in the magnetic case.

Table 1. The proportionality coefficients in our simulations with $B_\star$=0.5 kG and 1 kG.

B(kG)	0.5	1
coef.	R=6 | R=15	R=6 | R=15
$k_{1i}\|k_{1o}$	0.9	1.2 | 0.29
$k_{2i}\|k_{2o}$	-0.01 | -0.006	$+1.2\times10^{-4}\|-2.9\times10^{-3}$
k_3	-2.65×10^{-4}	$-4.4\times10^{-3}\|-3.6\times10^{-5}$
k_4	0.255	0.255
$k_{5i}\|k_{5o}$	-0.69 | -0.41	-1.25
$k_{6i}\|k_{6o}$	-0.35 | -0.15	-0.29 | -0.19
$k_{7i}\|k_{7o}$	-2.8 | -1.1	-8.2 | -1.18
k_8	5.8×10^{-3}	$8.\times10^{-3}$
k_9	0.01	0.01
ζ_1	5.	5.
ζ_2	0.5	0.5
ζ_8	5.	6.8
ζ_9	6.	4.5

Difference between analytical expressions and numerical simulations

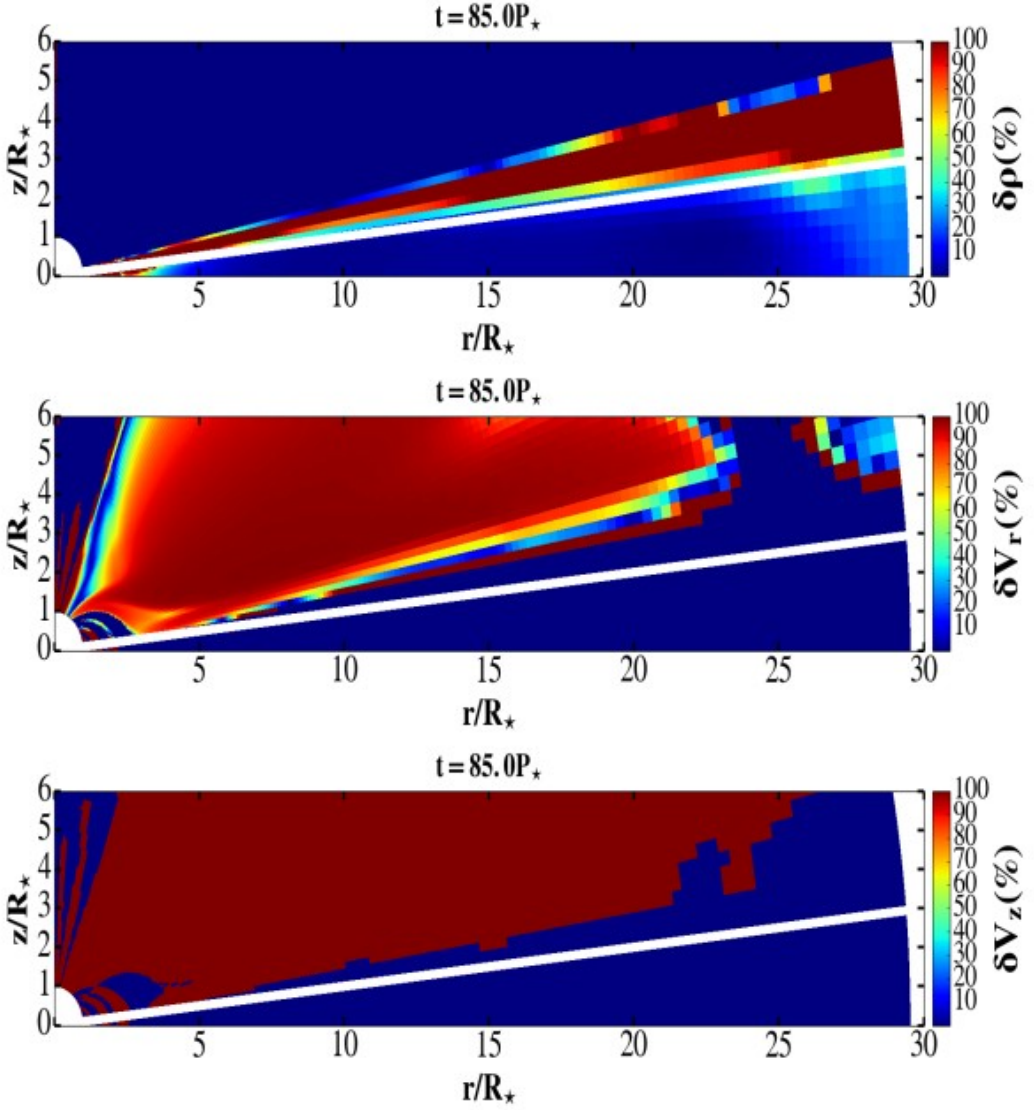

Fig. A.1. Difference between our numerical solutions and analytical expressions, in percentage of the value in the simulations. Our analytical solution is mostly inside the 10% margin everywhere inside the thin disk region, below the thick white solid line demarcating $h = 0.1r$ dependence, where h is the disk height.

Trends in angular momentum with increasing stellar magnetic field

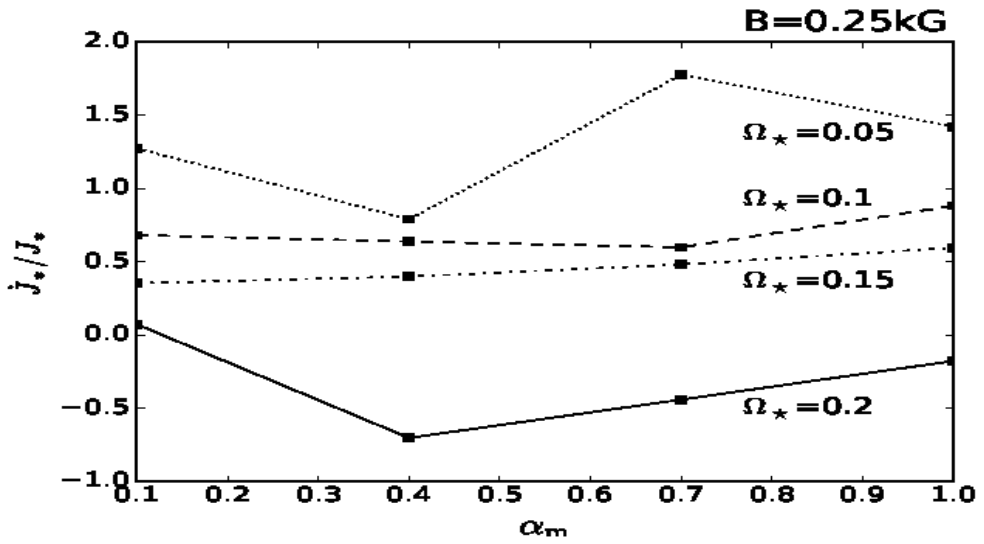

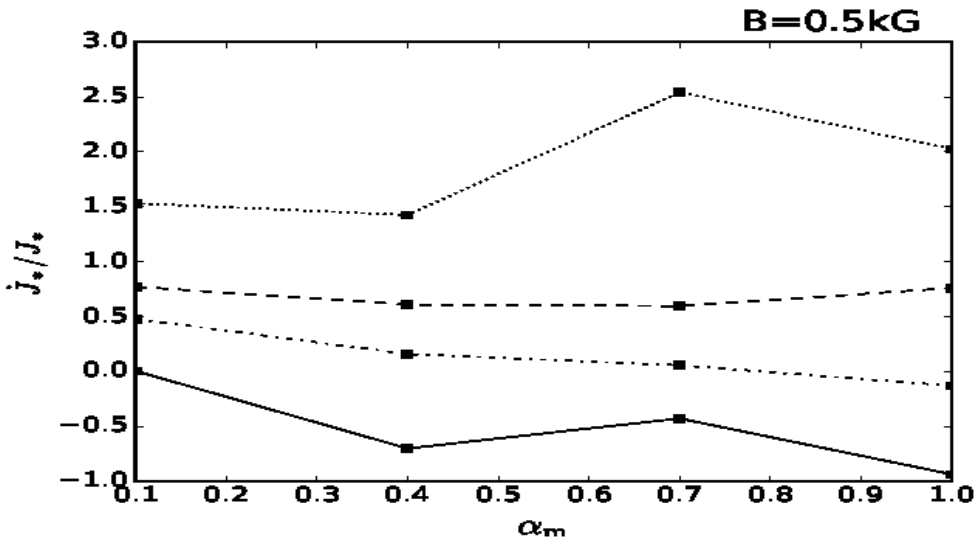

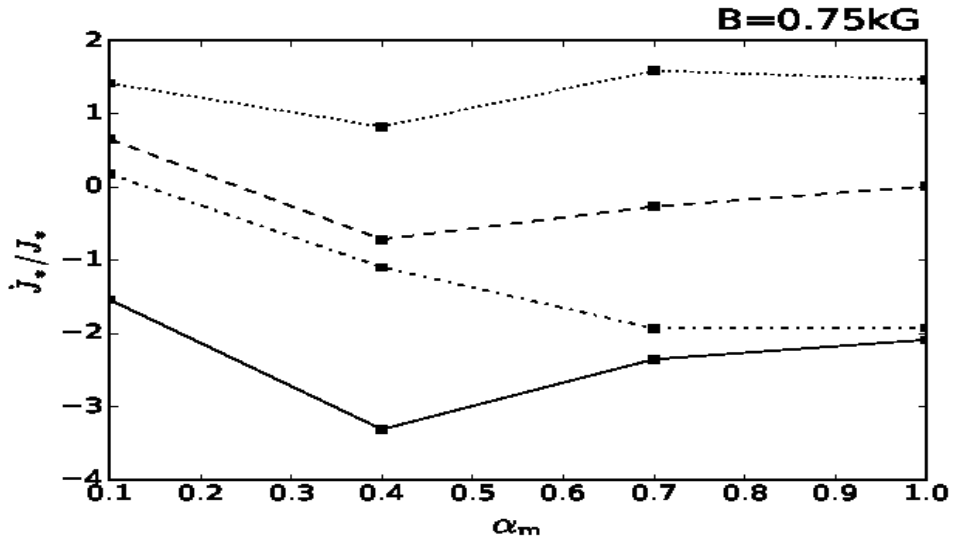

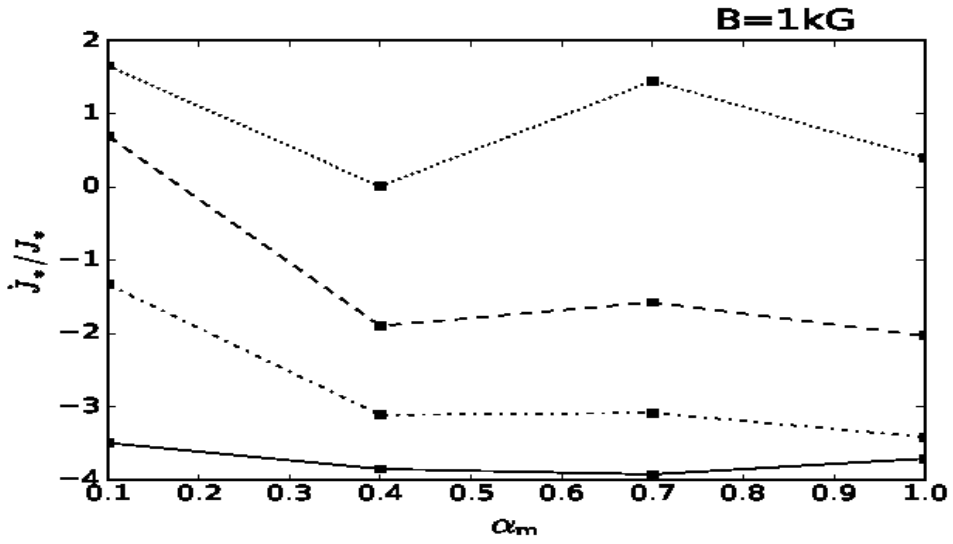

Average angular momentum flux transported onto the stellar surface by the matter in-falling from the disk onto the star through the accretion column. In each panel is shown a set of solutions with one stellar magnetic field strength, varying the stellar rotation rate and resistivity. Positive flux spins-up the star, negative slows it down. With the increase in stellar rotation rate, spin-up of the star by the infalling matter decreases, eventually switching to the spin-down.

Trends in angular momentum

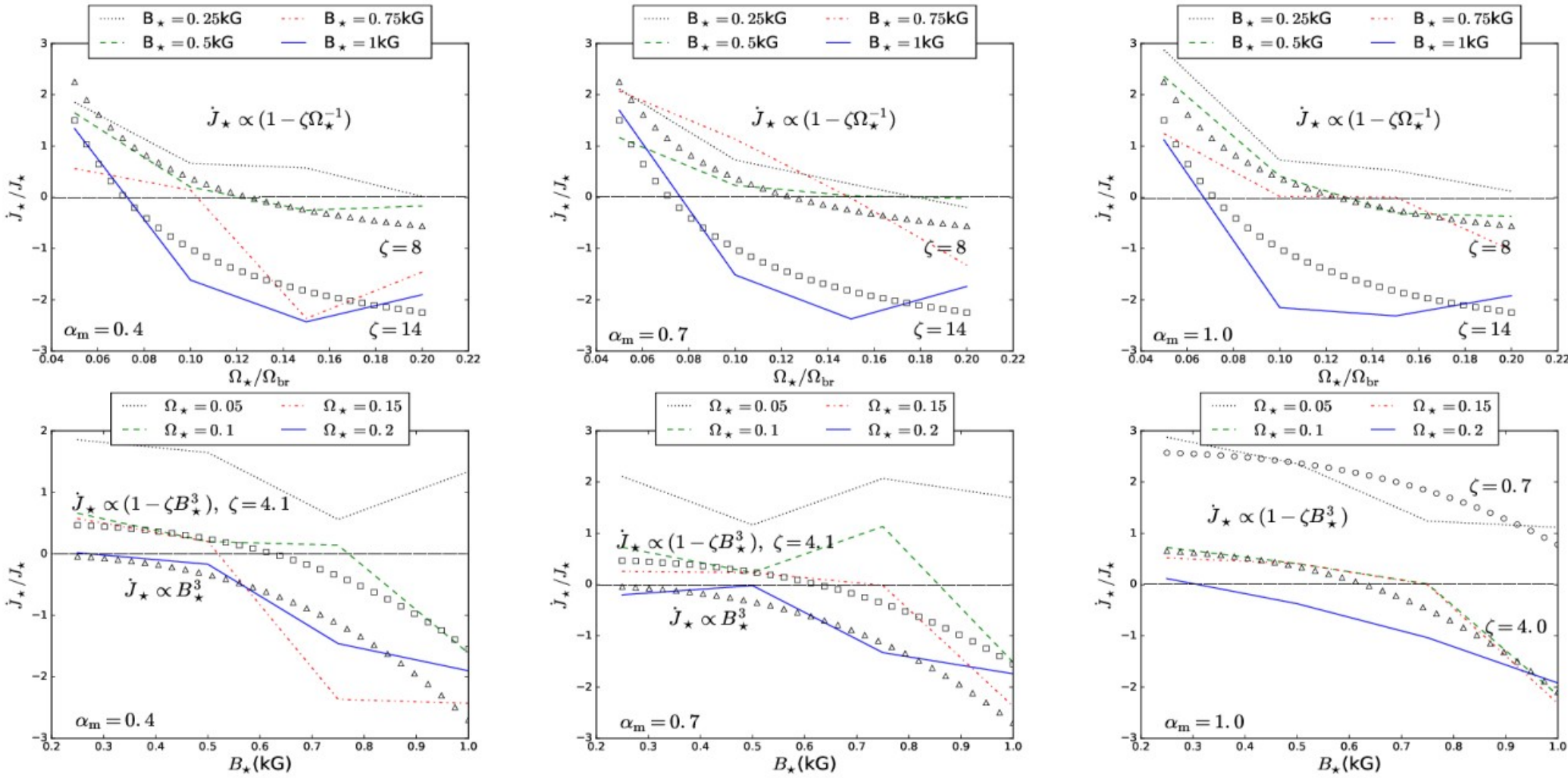

Fig. 7. Torques exerted on the star by material in-falling from the disk in all the cases without conical outflow-this are all the cases except a,b,c,d(1,5,9,13)-with the resistive coefficient $\alpha_{\rm m}$=0.4, 0.7 and 1.0. Approximate matching functions and trends in solutions with different stellar rotation rates and magnetic field strengths are shown as $\dot{J}_\star(\Omega_\star)$ (top panels) and $\dot{J}_\star(B_\star)$ (bottom panels).

Axial outflow (“jet”) launching

In the cases with faster stellar rotation, we obtain a continuous launching of an axial outflow from the star-disk magnetosphere.

The axial jet and the conical outflow are similar to the results in Romanova et al. (2009) and Zanni & Ferreira (2013).

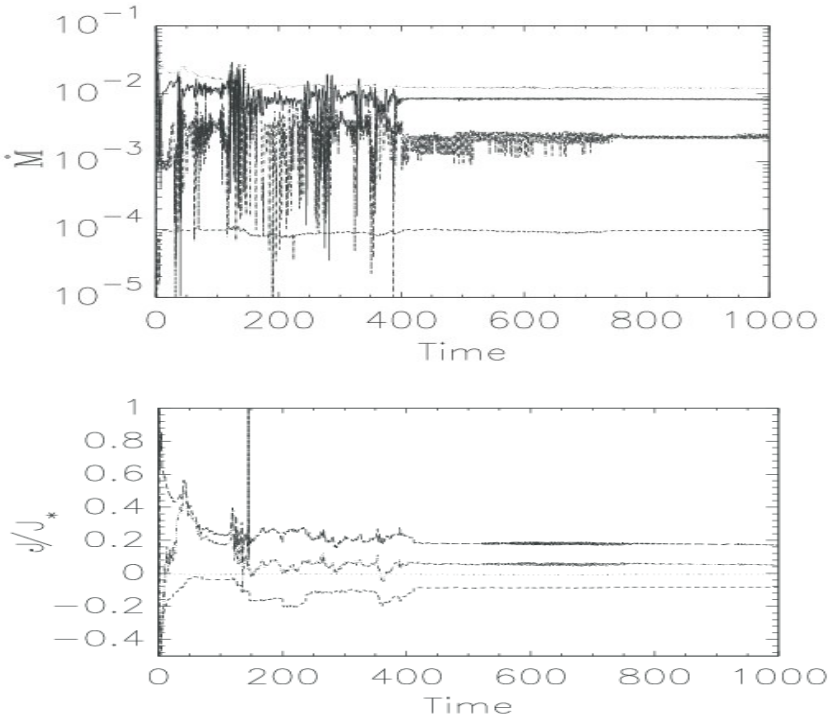

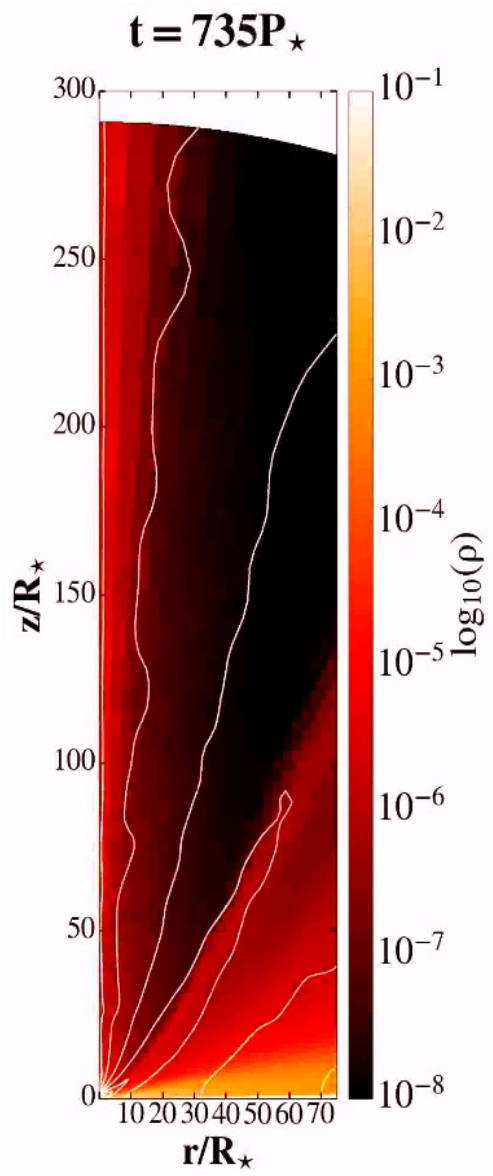

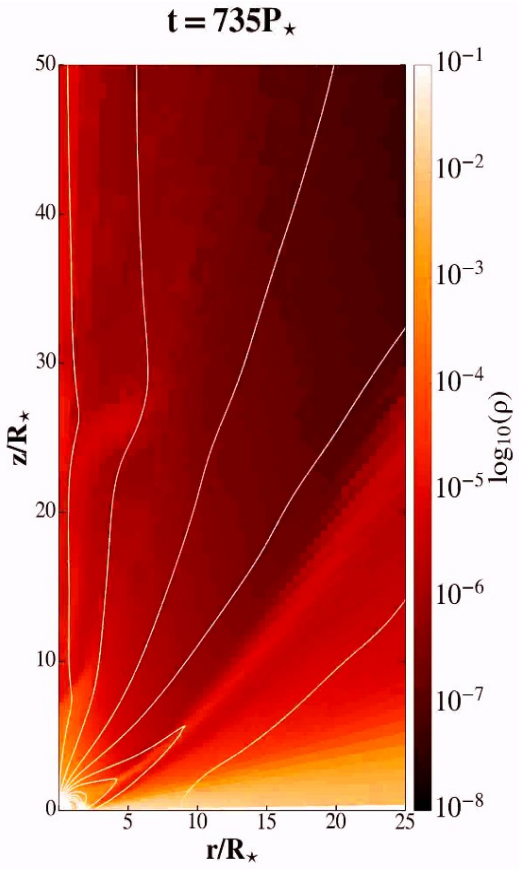

Zoom into the launching region.

Long lasting simulations-5s for millisecond pulsar

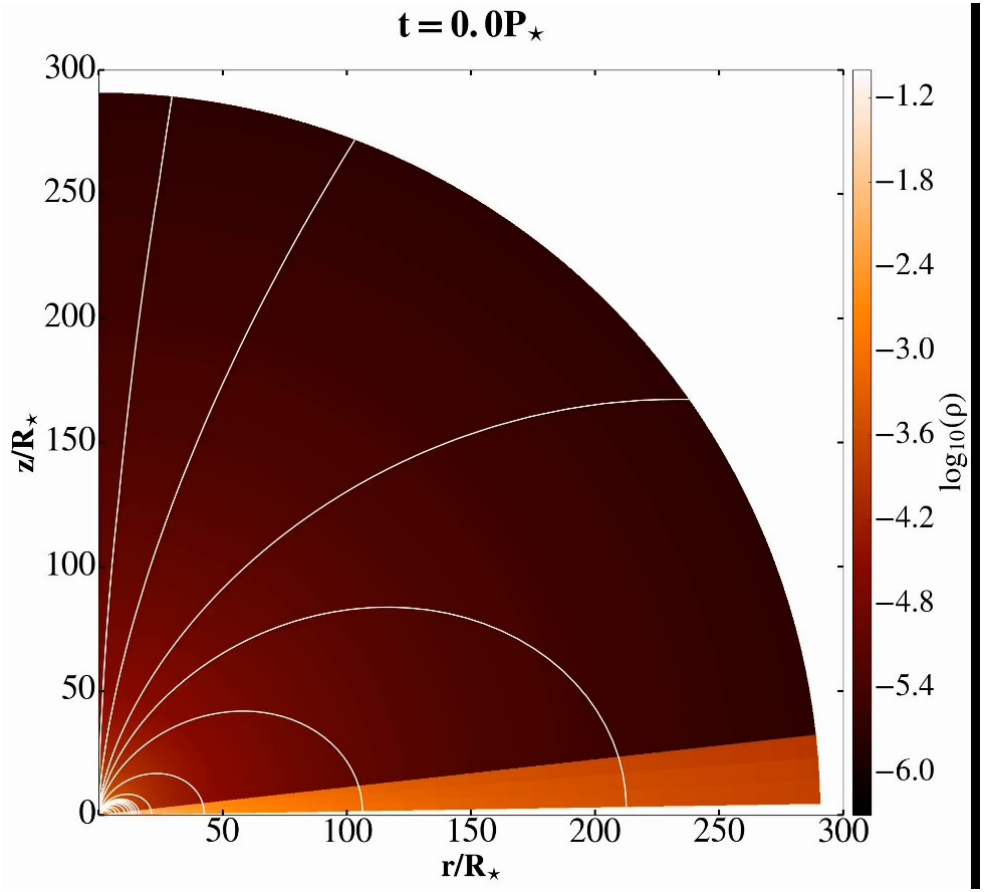

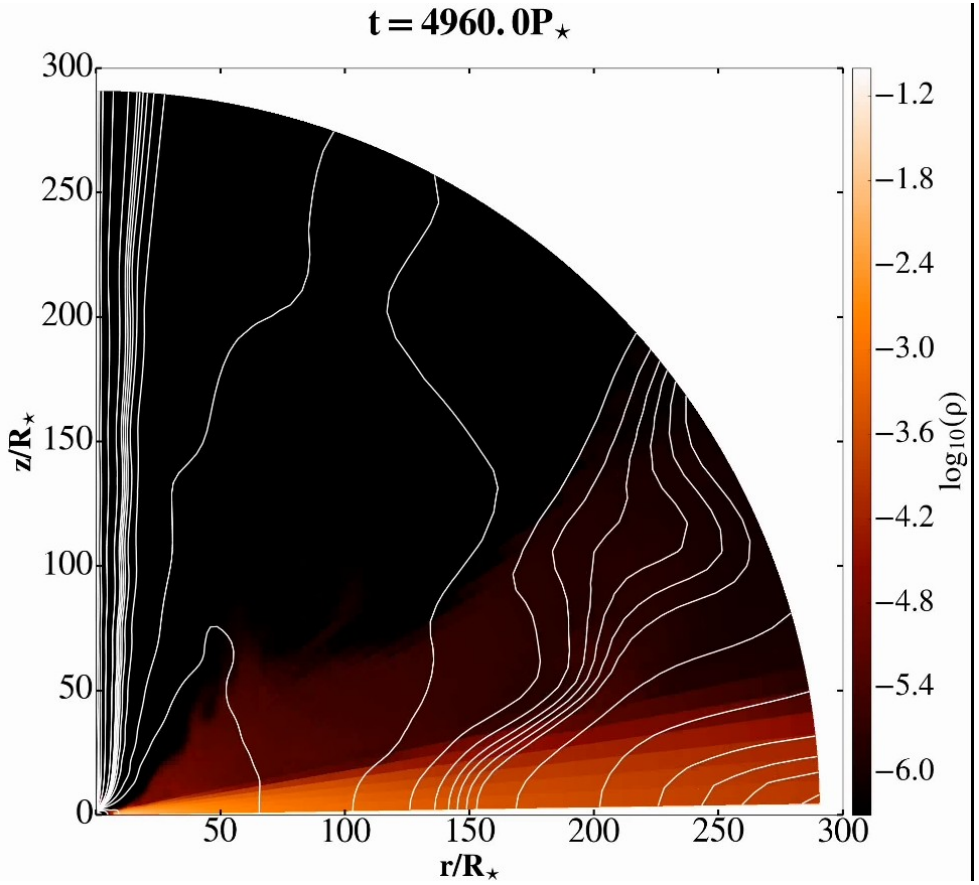

Light curve hiccups

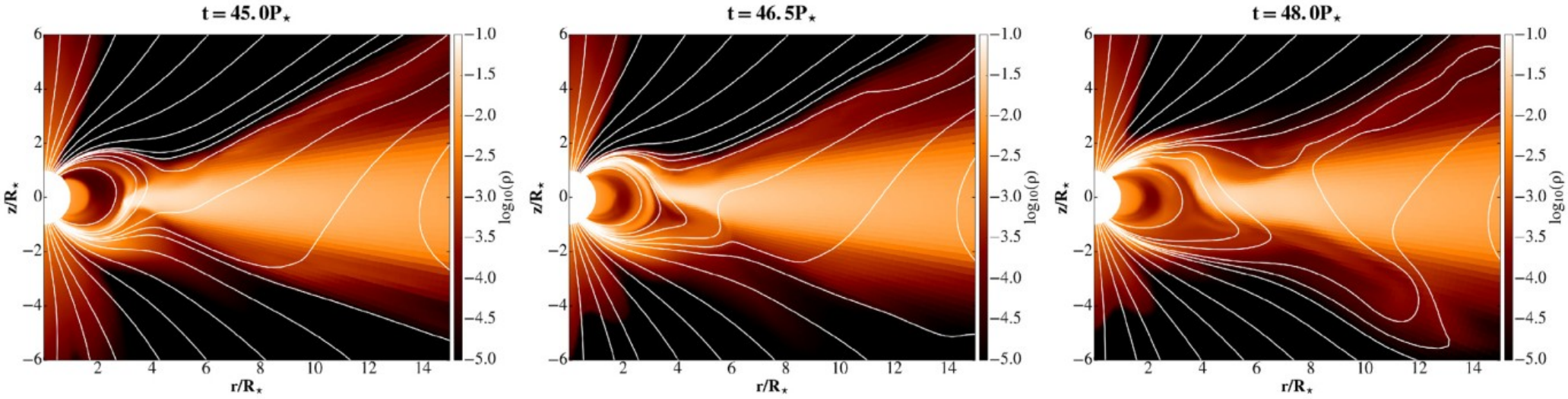

Figure 4. A sequence of snapshots from the results in the interval when switching of the accretion column from the Southern to the Northern hemisphere occurs.

Light curve hiccups

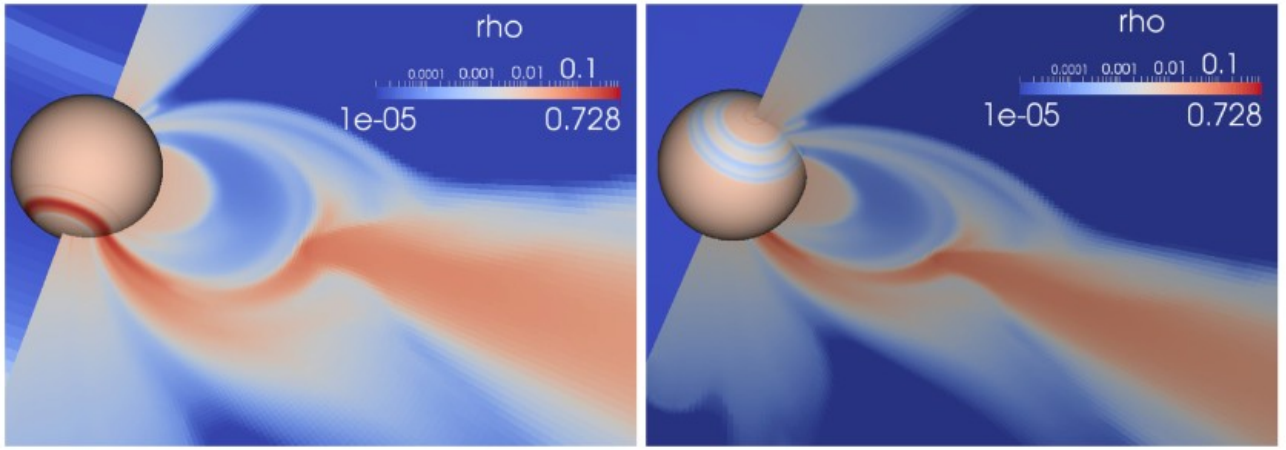

Figure 5. Snapshots in our 3D model from 2D axisymmetric simulations at $T = 45$ stellar rotations, with a cut in the meridional plane to show the accretic column and disc. In the left-hand panel is shown a view to the Southern hemisphere, with a ring-shaped hotspot at the footpoints of the accretion column. I the right-hand panel is shown a view to the Northern hemisphere, with a less dense ring-shaped hotspot than in the Southern hemisphere.

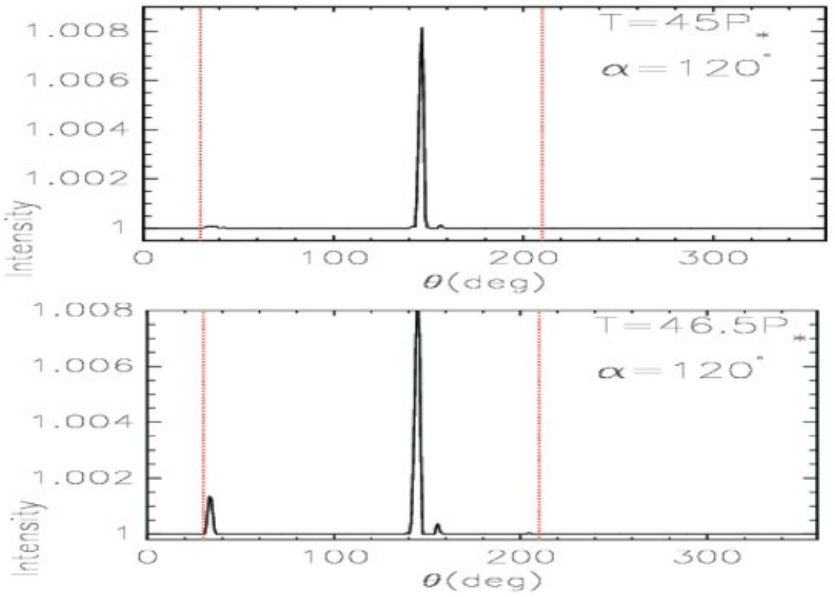

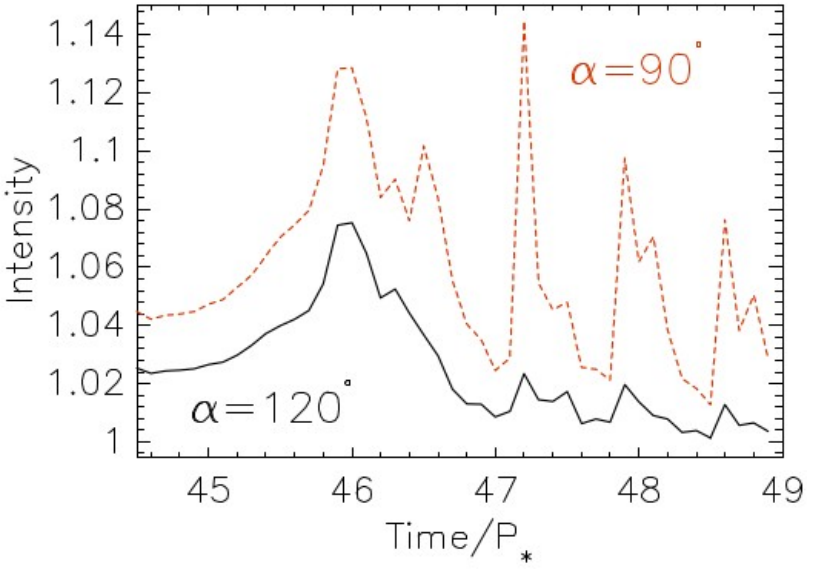

Light curve hiccups

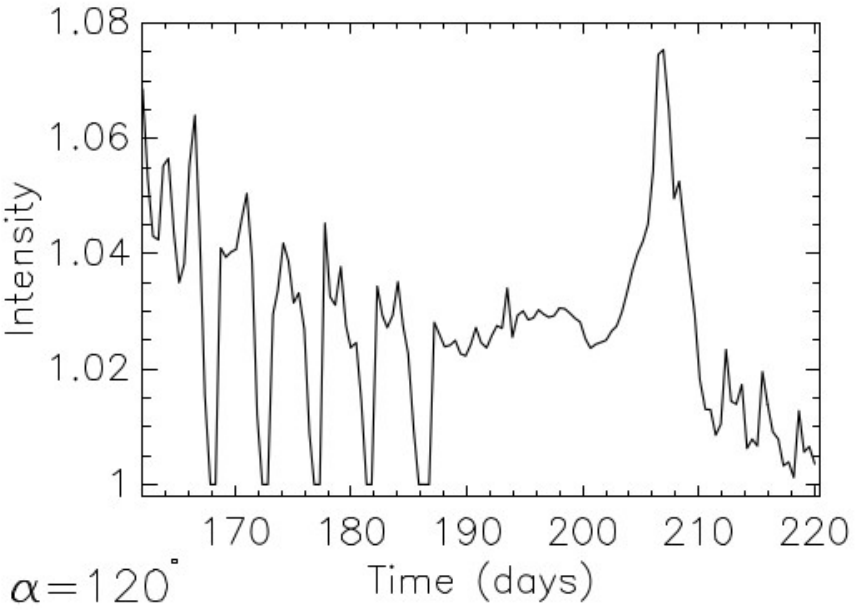

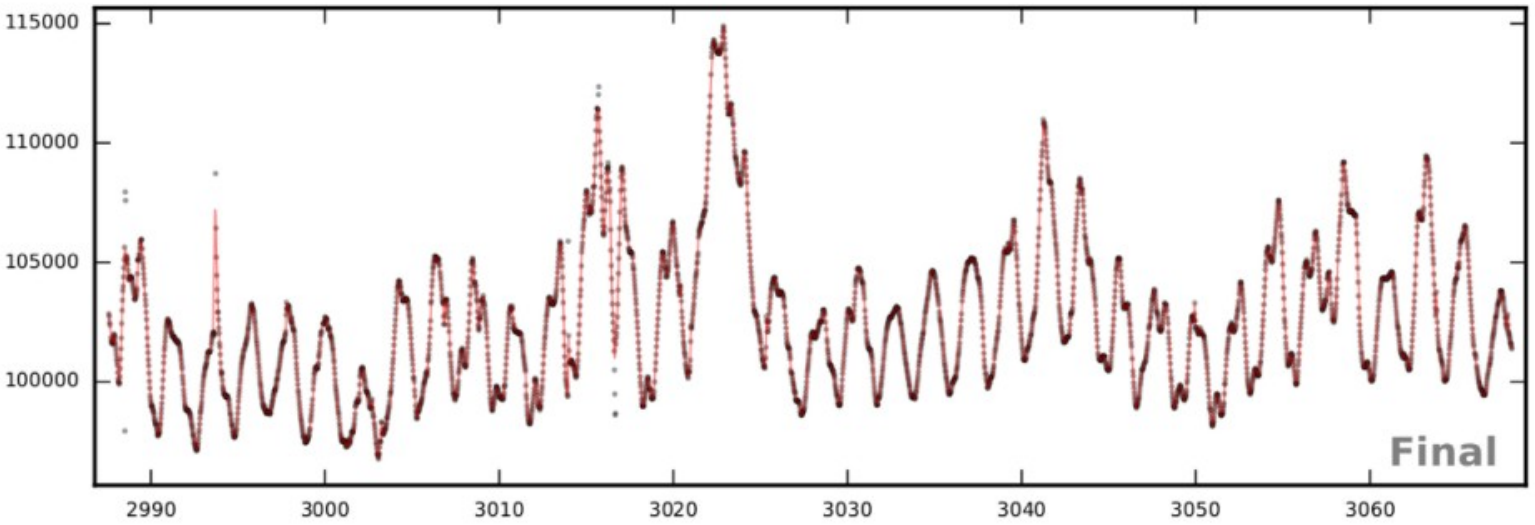

Figure 8. Top panel: intensity in a 3D model made from the longer time sequence than shown in Fig. 7. Shifts in the phase of the observed light ('hiccups') occur during the switch of the accretion column from the southern to northern stellar hemisphere between the 190 and 210 d. Bottom panel: light curve from the *Kepler* observation of V1000 Tau in which part of the contribution could occur because of the column switching. Time in the abscissa is annotated in Julian days.

Star-disk interaction with other geometries of the magnetic field

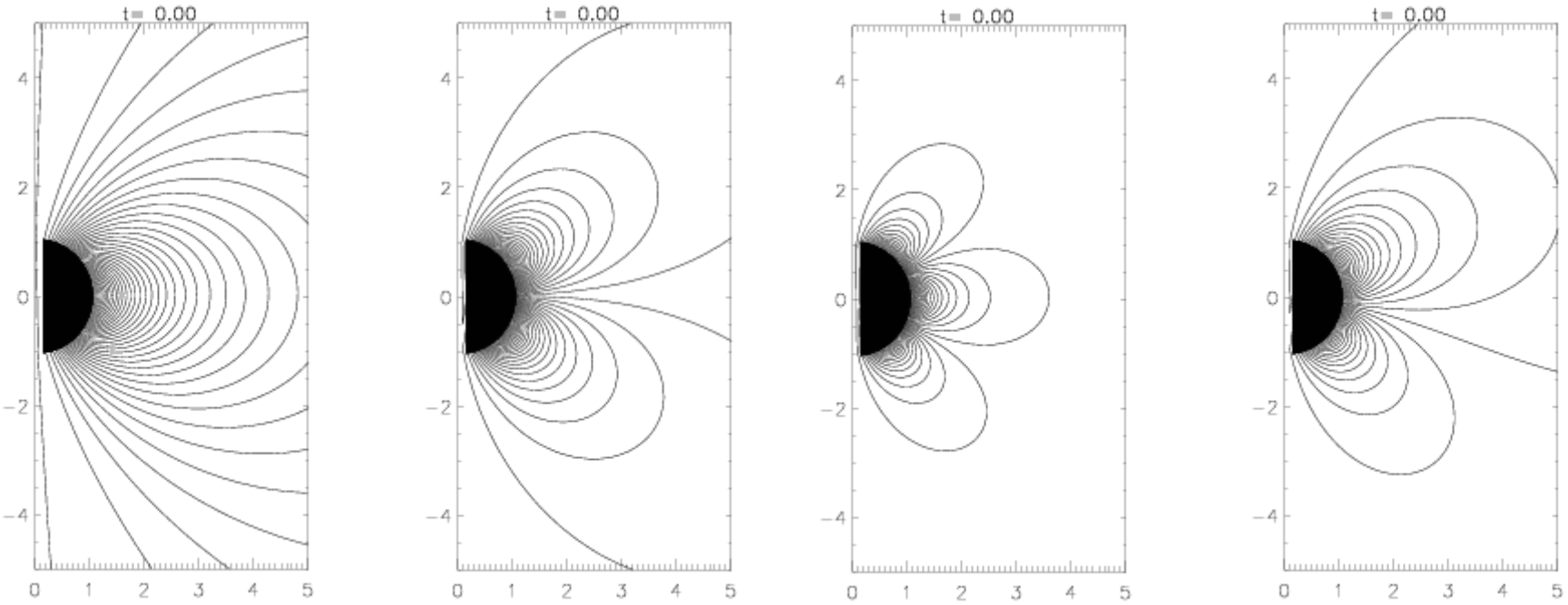

- In addition to the stellar dipole field, we also performed simulations with quadrupole, octupole and multipole fields.

Solutions with other geometries of the magnetic field

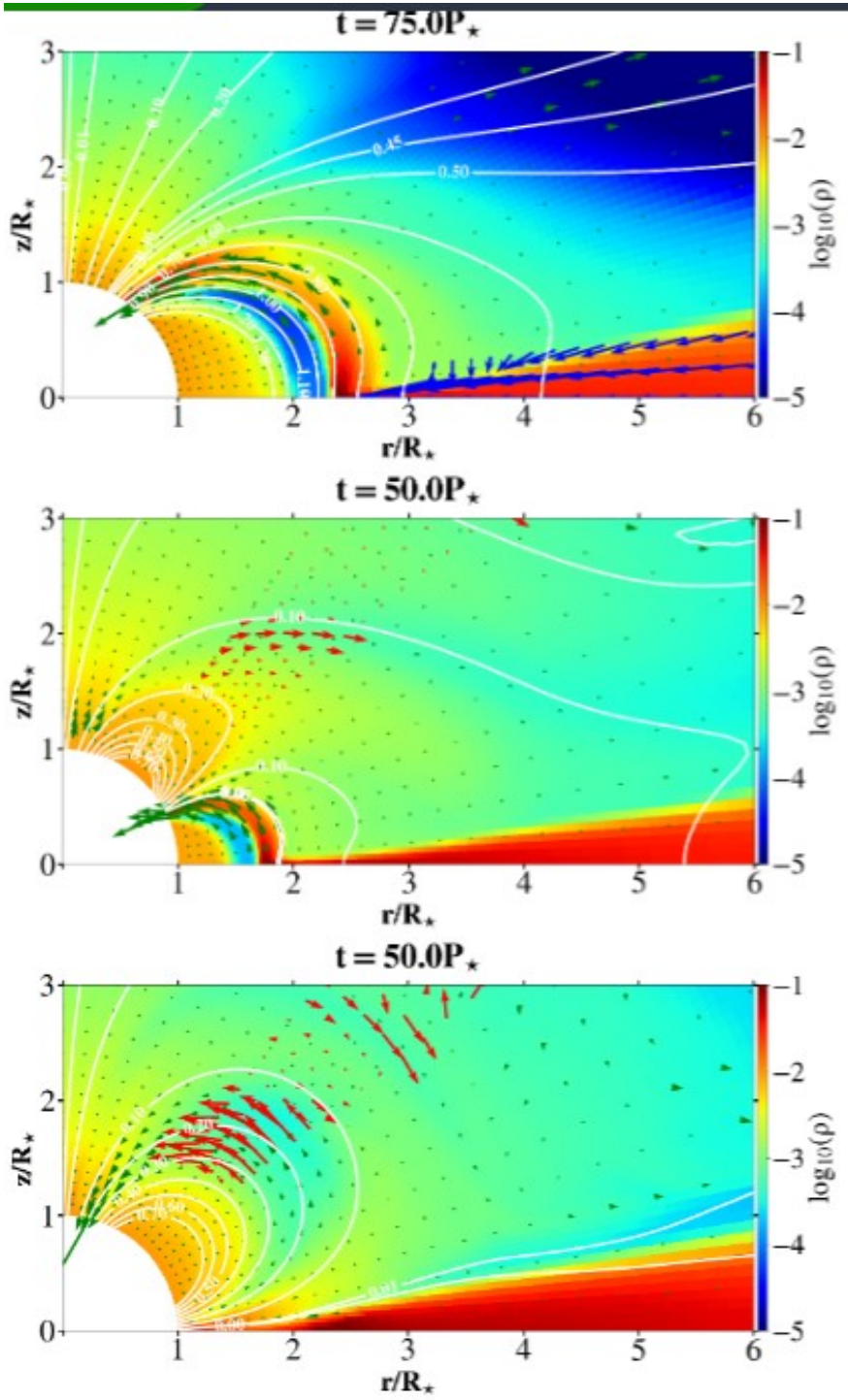

Figure: Zoom into the vicinity of the star in quasi-stationary results in our simulations with 0.5 kG stellar field, $\alpha_v = 1$, $\alpha_m = 1$ and stellar rotation rate $\Omega = 0.1\Omega_{br}$. Shown are the cases with the dipole, octupole and quadrupole stellar fields, in the top to bottom panels. The density is shown in the logarithmic color grading, poloidal magnetic field lines are shown with white solid lines, and vectors of poloidal velocity are multiplied with the factors 15 (in the disk) and 3 (in the corona) for better visibility.

Cieciuch and Cemeljic (2021, in preparation).

Summary

-The purely hydro-dynamic analytical solutions for a thin disk are available (Kluzniak-Kita 2000).

- -Viscous and resistive MHD star-disk magnetospheric interaction solutions for a thin accretion disk are available for young stellar objects. To some extent they are re-scalable to other objects with the same configuration.

-A quasi-stationary state is obtained in a set of 64 simulations with slowly rotating stars (up to 0.2 of the breakup stellar rotation rate).

-Results are compared to find trends for angular momentum in the solutions.

-In the cases with α_m=0.1, a conical outflow is launched.

-In the cases with faster rotating stars than those in our present parameter study, an axial outflow can be launched.

- I show an example of actual comparison with the light curve of the young stellar object.
- We also performed simulations with other geometries of the stellar magnetic field.